

See discussions, stats, and author profiles for this publication at: <https://www.researchgate.net/publication/358115209>

# Tight-binding Model in First and Second Quantization for Band Structure Calculations

Article in *Brazilian Journal of Physics* · April 2022

DOI: 10.1007/s13538-021-01027-x

---

CITATION

1

READS

1,385

---

5 authors, including:



Wellisson Pires Lima  
Universidade Federal do Ceará

2 PUBLICATIONS 1 CITATION

[SEE PROFILE](#)



Francisco Ronan Viana Araújo

Instituto Federal do Piauí (IFPI)

8 PUBLICATIONS 8 CITATIONS

[SEE PROFILE](#)



Diego Da Costa  
Universidade Federal do Ceará

64 PUBLICATIONS 895 CITATIONS

[SEE PROFILE](#)



S. H. R. Sena

Universidade da Integração Internacional da Lusofonia Afro-Brasileira (Unilab)

11 PUBLICATIONS 152 CITATIONS

[SEE PROFILE](#)

Some of the authors of this publication are also working on these related projects:



Electronic and transport properties in two-dimensional anisotropic semiconductor materials [View project](#)



Thermodynamics [View project](#)



# Tight-binding Model in First and Second Quantization for Band Structure Calculations

W. P. Lima<sup>1</sup>  · F. R. V. Araújo<sup>1,2</sup> · D. R. da Costa<sup>1</sup> · S. H. R. Sena<sup>3</sup> · J. M. Pereira Jr.<sup>1</sup>

Received: 30 August 2021 / Accepted: 23 November 2021

© The Author(s) under exclusive licence to Sociedade Brasileira de Física 2022

## Abstract

In this paper, we review the tight-binding model in the first and second quantization and show how it can be used to calculate the energy spectrum of some crystals. From an approach based on the Schrödinger equation (first quantization), we demonstrate the procedure for writing a generic Hamiltonian in the second quantization formalism. The connection between these two formalisms is generally not discussed in technical and applied works. As application examples, we use both methodologies to calculate the energy spectrum of a linear chain and a square lattice analytically, initially considering only one site per unit cell and later taking two sites per unit cell. Next, we apply the tight-binding model to graphene and compare such description with the brick lattice, showing that graphene lattice can be mapped as a square lattice with some hopping parameters being neglected. Finally, we apply the model to the  $\tau_3$ -lattice, a three-band system. In all cases, we present the energy spectrum and the density of states.

**Keywords** Electronic properties · Tight-binding model · First quantization · Second quantization · Two-dimensional crystals

## 1 Introduction

Quantum mechanics is rightly seen as one of the greatest triumphs of the twentieth-century theoretical physics. The theory explained not only several experimental results that had baffled researchers at the beginning of the last century,

but it also made important predictions that were later verified and are now recognized as the microscopic basis for all chemistry and materials science. However, soon after elaborating the first mathematically consistent formalism of quantum mechanics, it was realized that one would often face apparently insurmountable difficulties to obtain results from the theory. That first becomes evident as one tries to apply the theory to the problem of the energy spectrum of atoms heavier than hydrogen, even disregarding the dynamics of the nucleus. In this case, the solution of the Schrödinger's equation is complicated since the wave function is dependent on  $3N$  variables, with  $N$  being the number of electrons in the system, and the potential involves the electron-electron Coulomb interaction, apart from the coupling with the nucleus. Therefore, in order to calculate the properties of atoms and molecules, one is forced to use analytical approximations and numerical approaches, such as density functional theory [1], which frequently lead to time-consuming numerical calculations.

Thus, it may come as a surprise that in the case of solids, simple and accurate approximations have been found, allowing the prediction of several properties of these systems. This is due to some aspects of the physics of materials that seem to conspire to allow the calculation of electronic structures in a relatively simple way. The first is that crystals are

<sup>1</sup> Departamento de Física, Campus do Pici, Universidade Federal do Ceará, 60455-900 Fortaleza, CE, Brazil

<sup>2</sup> Campus São Raimundo Nonato, Instituto Federal do Piauí, 64670-000 São Raimundo Nonato, PI, Brazil

<sup>3</sup> Instituto de Ciências Exatas e da Natureza, Universidade da Integração Internacional da Lusofonia Afro-Brasileira, 62790-000 Redenção, CE, Brazil

characterized by having atoms sitting in a periodic lattice, i.e., the lowest energy configuration consists of a repeating pattern which, in turn, creates a periodic electron–ion potential. The periodicity of the potential leads naturally to Bloch's theorem and the prediction of energy bands [2]. A second factor is the fermionic character of the electrons, which means that they must obey Pauli's exclusion principle. This principle prevents more than two electrons (allowing for spin degeneracy) from occupying the same energy levels. Consequently, as more atoms are added to the system the total number of electrons increases, and those have to occupy even higher energies, up to a certain level, known as the Fermi energy. Thus, for many properties of interest such as thermal and electronic transport in crystals, only the highest energy states are relevant, viz. states with energies close to the Fermi level. It also happens that, for electrons with total energies in that range, their kinetic energies will usually far surpass the electron–electron interaction energies. This means that for these electrons, the coupling between electrons can often be disregarded. Moreover, since the periodic lattice potential is obtained from atomic potentials, this causes the lower-energy electrons to be more strongly bound to the host atoms, resulting in that the dynamics of the so-called core electrons can often be neglected in the calculations as well.

Therefore, one is left with a picture of (approximately) independent electrons moving in a periodic potential generated by the ionic cores. The wave functions of those independent electrons can be written as linear combinations of the orbitals of isolated atoms [3], an approximation that can be justified by assuming that each electron is strongly bound to a single core, with some probability of tunneling to neighboring sites in the lattice. Such approximation is thus known as a tight-binding (TB) model. An important property of such models is that they allow the inclusion of additional terms, such as electron–electron coupling, electron–phonon or spin–orbit interaction terms in a systematic way, as corrections to the single-particle picture.

By employing such a model, a fairly comprehensive understanding of solids can be obtained. In this paper, we show a brief introduction of TB models applied to 1D and 2D materials. Quasi-two-dimensional systems contain a single or a few layers of crystalline atoms and have first been brought to attention due to graphene production in 2004 [4]. Since then, various lamellar crystals have been produced, which have been modeled using TB models that provide a good description of the energy bands in the vicinity of the Fermi level. The paper is organized as follows: In Sect. 2 (3), we present the first (second) quantization formalism for the TB model. In Sect. 4, we show the equivalences between the first and second quantization formalisms of the TB model. In Sect. 5, we describe a procedure that can be used to obtain the band structure of some materials, as done in Sect. 6 for five crystal lattices, namely linear chain, square lattice, brick lattice (square lattice model

of graphene), graphene and  $\tau_3$ -lattice. We summarize our main findings and draw some perspectives in Sect. 7.

## 2 First Quantization Formalism

The TB model consists of writing the electron's wave function as a linear combination of atomic orbitals, with procedure name being in abbreviated format as LCAO, taking into account the various sites of a given crystal. Thus, in the TB model, states and energies in a crystal are determined from localized atomic orbitals. We assume that the electron is strongly bound to the nucleus in these orbitals, which means that it is confined to a region of small dimensions compared to internuclear distances. It is an approach that successfully describes several materials [5–8], making it possible to obtain different electronic and transport properties [9–13]. Despite being a reasonably simple model, it can take into account complex phenomena, such as the quantum Hall effect in graphene with an AC electric field [14].

In the following subsections, we present a procedure to determine the eigenvalues of the Hamiltonian by the first quantization formalism within the TB model.

### 2.1 Linear Combination of Atomic Orbitals

Let us assume that in the vicinity of each lattice site the total Hamiltonian  $\mathcal{H}$  can be approximated by the Hamiltonian of the localized atoms,  $\mathcal{H}_{at}$ . Additionally, it is also assumed that the bound levels of the atomic Hamiltonian,  $\varphi_j(\mathbf{r})$ , are well localized, so that

$$\mathcal{H}_{at}\varphi_j(\mathbf{r}) = \varepsilon_j\varphi_j(\mathbf{r}), \quad (1)$$

where  $\varepsilon_j$  are energy eigenvalues and  $\varphi_j(\mathbf{r})$  will be negligible when  $|\mathbf{r}|$  exceeds a distance of the order of the lattice parameter. One can improve the approximation by considering the case where  $|\mathbf{r}|$  is comparable to the lattice parameter. For this, one can include an additional term,  $\Delta U(\mathbf{r})$ , to the Hamiltonian of the localized atoms containing all corrections to the atomic potential necessary to produce the periodic potential of the crystal:

$$\mathcal{H} = \mathcal{H}_{at} + \Delta U(\mathbf{r}). \quad (2)$$

In this case, taking an atom localized at the origin, the wave function  $\varphi_j(\mathbf{r})$  will be a good approximation to a steady-state wave function for the total Hamiltonian, with energy eigenvalues  $\varepsilon_j$  [15]. Likewise, the wave functions  $\varphi_j(\mathbf{r} - \mathbf{R})$  will be good approximations for the corresponding sites  $\mathbf{R}$  of the Bravais lattice.

Since, by assumption,  $\varphi_j(\mathbf{r})$  satisfies the Schrödinger equation for the localized atoms [Eq. (1)], it must also satisfy the Schrödinger equation for the total Hamiltonian

[Eq. (2)], whenever  $\Delta U(\mathbf{r})$  is null and  $\varphi_j(\mathbf{r})$  is non-null. In this situation, each atomic level  $\varphi_j(\mathbf{r})$  of the localized atoms gives rise to  $N$  levels in the periodic potential of the crystal, with wave functions  $\varphi_j(\mathbf{r} - \mathbf{R})$ , since  $N$  is the number of unit cells. Thus, one needs to find the  $N$  linear combinations of these states that represent the Bloch function  $\Phi_j(\mathbf{r}, \mathbf{k})$  that describe the electrons in the crystal, i.e.,

$$T_{\mathbf{R}}\Phi_j(\mathbf{r}, \mathbf{k}) = e^{i\mathbf{k}\cdot\mathbf{R}}\Phi_j(\mathbf{r}, \mathbf{k}), \quad (3)$$

where  $T_{\mathbf{R}}$  is the translation operation along the lattice vector  $\mathbf{R}$ . At this point, the main assumption of the TB method emerges, i.e., to assume that the Bloch function can be given in terms of the atomic orbitals:

$$\Phi_j(\mathbf{r}, \mathbf{k}) = \frac{1}{\sqrt{N}} \sum_{\mathbf{R}} e^{i\mathbf{k}\cdot\mathbf{R}} \varphi_j(\mathbf{r} - \mathbf{R}), \quad j = 1, 2, \dots, n, \quad (4)$$

where  $n$  is the number of atomic wave functions in the unit cell, and we have  $n$  Bloch functions in the solid for a given  $\mathbf{k}$ . For each state  $j$ , one takes the contribution of the  $N$  corresponding localized atoms, weighted by a phase factor  $e^{i\mathbf{k}\cdot\mathbf{R}}$  in the Bravais lattice, with the term  $1/\sqrt{N}$  being a normalization constant [16].

Although the wave function (4) satisfies Bloch's theorem for a given  $\mathbf{k}$ , it represents only the electronic characteristics of localized atoms, requiring modifications to fully represent the electrons in the crystal. As a first approximation, we consider that  $\Delta U(\mathbf{r})$  would vanish whenever  $\varphi_j(\mathbf{r})$  was nonzero. However, a more realistic assumption is that  $\varphi_j(\mathbf{r})$  becomes small but not exactly null before  $\Delta U(\mathbf{r})$  becomes appreciable [15]. Thus, the wave function that describes the electrons in the crystal can be similar to the Bloch function, given by:

$$\Psi_j(\mathbf{r}, \mathbf{k}) = \frac{1}{\sqrt{N}} \sum_{\mathbf{R}} e^{i\mathbf{k}\cdot\mathbf{R}} \psi_j(\mathbf{r} - \mathbf{R}), \quad j = 1, 2, \dots, n, \quad (5)$$

with  $\psi_j(\mathbf{r} - \mathbf{R})$  to be determined and being not necessarily an exact atomic steady-state wave function. Considering  $\Delta U(\mathbf{r})\varphi_j(\mathbf{r})$  very small, but different from zero, we can write  $\psi_j(\mathbf{r} - \mathbf{R})$  as a linear combination of localized atomic wave functions:

$$\psi_j(\mathbf{r} - \mathbf{R}) = \sum_{j'} C_{jj'} \varphi_{j'}(\mathbf{r} - \mathbf{R}), \quad (6)$$

where  $C_{jj'}$  are complex coefficients to be found. To better understand that, note from Eqs. (5) and (6) that

$$\begin{aligned} \Psi_j(\mathbf{r}, \mathbf{k}) &= \frac{1}{\sqrt{N}} \sum_{\mathbf{R}} e^{i\mathbf{k}\cdot\mathbf{R}} \sum_{j'} C_{jj'} \varphi_{j'}(\mathbf{r} - \mathbf{R}) \\ &= \sum_{j'} C_{jj'} \frac{1}{\sqrt{N}} \sum_{\mathbf{R}} e^{i\mathbf{k}\cdot\mathbf{R}} \varphi_{j'}(\mathbf{r} - \mathbf{R}), \end{aligned} \quad (7)$$

and using Eq. (4), we have [16]

$$\Psi_j(\mathbf{r}, \mathbf{k}) = \sum_{j'} C_{jj'} \Phi_{j'}(\mathbf{r}, \mathbf{k}), \quad (8)$$

and therefore, the wave function that describes the electrons in the crystal,  $\Psi_j(\mathbf{r}, \mathbf{k})$ , is ultimately a linear combination of the atomic orbitals  $\varphi_{j'}(\mathbf{r} - \mathbf{R})$ .

## 2.2 Secular Equation

The energy eigenvalues  $E_i = E_i(\mathbf{k})$  of the total Hamiltonian  $\mathcal{H}$  are given by

$$E_i = \frac{\langle \Psi_i | \mathcal{H} | \Psi_i \rangle}{\langle \Psi_i | \Psi_i \rangle}. \quad (9)$$

Replacing Eq. (8) into Eq. (9), we obtain

$$E_i = \frac{\sum_{j,j'} \mathcal{H}_{jj'} C_{ij}^* C_{ij'}}{\sum_{j,j'} \mathcal{S}_{jj'} C_{ij}^* C_{ij'}}, \quad (10)$$

where the integrals over the Bloch orbitals,  $\mathcal{H}_{jj'} = \mathcal{H}_{jj'}(\mathbf{k})$  and  $\mathcal{S}_{jj'} = \mathcal{S}_{jj'}(\mathbf{k})$ , are called the transfer integral matrices and overlap integral matrices [16], or simply transfer [17, 18] and overlap matrices, respectively, and are defined by

$$\mathcal{H}_{jj'} = \langle \Phi_j | \mathcal{H} | \Phi_{j'} \rangle, \quad j, j' = 1, 2, \dots, n, \quad (11)$$

$$\mathcal{S}_{jj'} = \langle \Phi_j | \Phi_{j'} \rangle, \quad j, j' = 1, 2, \dots, n. \quad (12)$$

Substituting the Bloch function, Eq. (4), into Eq. (11), the transfer matrix elements become

$$\mathcal{H}_{jj'} = \frac{1}{N} \sum_{\mathbf{R}, \mathbf{R}'} e^{i\mathbf{k}\cdot(\mathbf{R}' - \mathbf{R})} t_{\mathbf{R}, \mathbf{R}'}^{jj'}, \quad (13)$$

where we define

$$t_{\mathbf{R}, \mathbf{R}'}^{jj'} = \langle \varphi_j(\mathbf{r} - \mathbf{R}) | \mathcal{H} | \varphi_{j'}(\mathbf{r} - \mathbf{R}') \rangle, \quad (14)$$

as the transfer integral or hopping parameter related to the interacting energy between electrons located on different sites [19] and usually has a negative value [16], i.e., this energetic term is associated with the energy required for an electron to "hop" from a site at position  $\mathbf{R}'$  to a given site at position  $\mathbf{R}$ , or vice versa. Note that  $j$  and  $j'$  are associated with different orbitals of the atomic sites at positions  $\mathbf{R}$  and  $\mathbf{R}'$ , being the mathematical notation with four indices necessary to avoid misleading. If the distance between the sites increases, then the corresponding hopping parameter is reduced in module. In general, the band structure is initially calculated by means of first principles methods and then a search is done for the hopping parameters that best fit the energy bands obtained by the TB method to those obtained by the first principles calculations [16], in a similar way as done in the Wannierization procedure of density functional theory [20].

Likewise, replacing the Bloch function, Eq. (4), into Eq. (12), the overlap matrix elements can be written as

$$\mathcal{S}_{jj'} = \frac{1}{N} \sum_{\mathbf{R}, \mathbf{R}'} e^{i\mathbf{k} \cdot (\mathbf{R}' - \mathbf{R})} s_{\mathbf{R}, \mathbf{R}'}^{jj'}, \quad (15)$$

where we define

$$s_{\mathbf{R}, \mathbf{R}'}^{jj'} = \langle \varphi_j(\mathbf{r} - \mathbf{R}) | \varphi_{j'}(\mathbf{r} - \mathbf{R}') \rangle, \quad (16)$$

as the overlap integral or overlap parameter, which represents the overlap between the atomic orbitals of the  $\mathbf{R}$  and  $\mathbf{R}'$  sites. For instance, if one considers the overlap parameter corresponding to the atomic orbitals of the  $\mathbf{R}$  and  $\mathbf{R}' = \mathbf{R}$  sites, one finds  $s_{\mathbf{R}, \mathbf{R}'}^{jj'} = \delta_{jj'}$ . In general, it is preferable to consider an orthonormal model, where  $s_{\mathbf{R}, \mathbf{R}'}^{jj'} = \delta_{\mathbf{R}\mathbf{R}'} \delta_{jj'}$ . In this situation, the overlap matrix will be the identity matrix. In a more general case, we have  $0 \leq s_{\mathbf{R}, \mathbf{R}'}^{jj'} \leq 1$ . Most of the applications of the TB method are found in the literature; usually one only takes into account the contributions of nearest neighbor (NN) sites for hopping and overlap parameters. However, a more accurate description must consider also contributions of more distant neighbors.

Let us now return to the discussion of Eq. (10). The complex coefficients  $C_{ij}^*$  are obtained so that the energy eigenvalues  $E_i$  are minimized [16], i.e., by doing

$$\begin{aligned} \frac{\partial E_i}{\partial C_{ij}^*} &= \frac{\sum_{j'} \mathcal{H}_{jj'} C_{ij'}}{\sum_{j,j'} \mathcal{S}_{jj'} C_{ij}^* C_{ij'}} \\ &\quad - \frac{\sum_{j,j'} \mathcal{H}_{jj'} C_{ij}^* C_{ij'}}{\left( \sum_{j,j'} \mathcal{S}_{jj'} C_{ij}^* C_{ij'} \right)^2} \sum_{j'} \mathcal{S}_{jj'} C_{ij'} = 0. \end{aligned} \quad (17)$$

Multiplying Eq. (17) by  $\sum_{j,j'} \mathcal{S}_{jj'} C_{ij}^* C_{ij'}$  and substituting Eq. (10) into Eq. (17), one obtains

$$\sum_{j'} \mathcal{H}_{jj'} C_{ij'} = E_i \sum_{j'} \mathcal{S}_{jj'} C_{ij'}. \quad (18)$$

Defining a column vector such as

$$C_i = \begin{pmatrix} C_{i1} \\ \vdots \\ C_{iN} \end{pmatrix}, \quad (19)$$

one can rewrite Eq. (18) as

$$\mathcal{H}C_i = E_i \mathcal{S}C_i \Rightarrow [\mathcal{H} - E_i \mathcal{S}]C_i = 0. \quad (20)$$

Note that if the inverse of the matrix  $[\mathcal{H} - E_i \mathcal{S}]$  exists, then we have

$$[\mathcal{H} - E_i \mathcal{S}][\mathcal{H} - E_i \mathcal{S}]^{-1} C_i = 0 \Rightarrow C_i = 0, \quad (21)$$

resulting in the trivial solution. However, we are only interested in the case where the matrix inverse does not exist, that is, in the case where  $[\mathcal{H} - E_i \mathcal{S}]$  is a singular matrix, therefore

$$\det[\mathcal{H} - E \mathcal{S}] = 0. \quad (22)$$

This equation, an important result of the TB method, is known as the secular equation. Due to the dimensionality  $n$  of the matrix  $\mathcal{H}$ , its solution provides  $n$  eigenvalues  $E_i$ 's with  $i = 1, \dots, n$ . In the case of an orthonormal TB model, the overlap matrix is the identity matrix, so that

$$\det[\mathcal{H} - E \mathcal{I}] = 0. \quad (23)$$

### 3 Hamiltonian in Second Quantization

The TB model in the first quantization as described above is sufficient to determine the band structure of crystals of interest. However, in the technical literature, the Hamiltonian is generally presented in second quantization, that is, in terms of creation and annihilation operators. In general, it is always possible to describe fermions in terms of such operators. Unlike bosons, fermions obey the Pauli exclusion principle. Representing an operator that creates (annihilates) an electron in the  $s$ -state by  $\hat{c}_s^\dagger$  ( $\hat{c}_s$ ) and defining an unoccupied state by  $|0\rangle$ , the Pauli exclusion principle imposes that  $\hat{c}_s^\dagger \hat{c}_s^\dagger |0\rangle = 0$  or equivalently  $\hat{c}_s^\dagger |1\rangle = 0$ . Other relations satisfied by operators  $\hat{c}_s^\dagger$  and  $\hat{c}_s$  are  $\hat{c}_s^\dagger |0\rangle = |1\rangle$ ,  $\hat{c}_s |1\rangle = |0\rangle$ , and  $\hat{c}_s |0\rangle = 0$ . In addition, the operator  $\hat{c}_s^\dagger \hat{c}_s$  provides the occupation of the  $s$ -state, that is,  $\hat{c}_s^\dagger \hat{c}_s |n\rangle = n|n\rangle$ , where  $n = 0, 1$ . The  $\hat{c}_s^\dagger$  and  $\hat{c}_s$  operators satisfy an anticommutation rule:  $\{\hat{c}_s, \hat{c}_s^\dagger\} = \hat{c}_s \hat{c}_s^\dagger + \hat{c}_s^\dagger \hat{c}_s = 1$ . In short, all these relations can be obtained using the following expressions [21]:

$$\{\hat{a}_r, \hat{a}_s^\dagger\} = \delta_{rs}, \quad \{\hat{a}_r, \hat{a}_s\} = 0, \quad \text{and} \quad \{\hat{a}_r^\dagger, \hat{a}_s^\dagger\} = 0. \quad (24)$$

Therefore, using the operators  $\hat{c}_s^\dagger$  and  $\hat{c}_s$ , we must begin our discussion by merely reformulating the Schrödinger equation in the language of second quantization. There are works in the literature that present the development of the second quantization formalism starting from the first quantization formalism [21, 22]. We call the general Hamiltonian the one that has not yet been reduced to the TB model, that is, the one that describes physical systems that do not necessarily obey the assumption of TB approximations discussed above. For this, one can consider the general Hamiltonian in the language of first quantization being written as

$$H = \sum_k T(x_k) + \frac{1}{2} \sum_{k \neq l} V(x_k, x_l), \quad (25)$$

where  $T \equiv T(x_k)$  is the kinetic energy,  $V \equiv V(x_k, x_l)$  is the potential energy of interaction between the particles, and  $x_k$  and  $x_l$  denote the coordinates of the  $k$ th and  $l$ th particles, respectively, including the spatial coordinate and any discrete variables, as for instance spin coordinates [21]. Using the algebra of the creation and annihilation operators, one can rewrite the general Hamiltonian (25) as [21]

$$\hat{H} = \sum_{ij} \hat{c}_i^\dagger \langle i | T | j \rangle \hat{c}_j + \frac{1}{2} \sum_{ijkl} \hat{c}_i^\dagger \hat{c}_j^\dagger \langle ij | V | kl \rangle \hat{c}_l \hat{c}_k, \quad (26)$$

where  $i$  and  $j$  are states that form a complete basis of Hilbert space in first quantization.  $\hat{H}$  is an operator in the abstract occupation-number space and, therefore, it is a general Hamiltonian in the language of second quantization.

By comparing Eqs. (25) and (26), it is seen that in the first quantization the kinetic and potential energies are written in terms of momentum and position operators. On the other hand, in the second quantization the operators of creation and annihilation are present. The transformation of the general Hamiltonian, initially written in terms of position and momentum operators, into occupation number representation is often called the second quantization procedure and is a useful formalism to describe and analyze quantum many-body systems.

In general, a generic one-body operator

$$J = \sum_i J(x_i), \quad (27)$$

written in first-quantized form, has its correspondent second-quantized operator given by [21]

$$\hat{J} = \sum_{ij} \langle i | J | j \rangle \hat{c}_i^\dagger \hat{c}_j. \quad (28)$$

Thus, neglecting the electron-electron interaction, we can write the general Hamiltonian in the second quantization admitting  $J = \mathcal{H}$  in Eq. (28), as

$$\hat{\mathcal{H}} = \sum_{ij} \langle i | \mathcal{H} | j \rangle \hat{c}_i^\dagger \hat{c}_j, \quad (29)$$

where  $i$  and  $j$  are generic wave functions. At this point, note that if the term  $\langle i | \mathcal{H} | j \rangle$  is associated with the hopping parameter  $t_{ij}$  [see Eq. (14)], with  $i$  and  $j$  representing atomic orbitals, then the general Hamiltonian (29) undergoes the TB approximation. Thus, the TB Hamiltonian in the second quantization is given by:

$$\hat{\mathcal{H}} = \sum_{ij} t_{ij} \hat{c}_i^\dagger \hat{c}_j. \quad (30)$$

In principle, the sum runs over all orbitals of all atomic sites that make up the crystallographic lattice. However, the number of neighbors, and consequently the number of hopping parameters, can be controlled, being the TB model more accurate as more nonvanishing hopping energies are taken into account. For example, the TB Hamiltonian that includes nearest-neighbor (NN) and next-nearest-neighbor (NNN) sites, with one orbital per site, can generally be written as

$$\hat{\mathcal{H}} = \sum_i E_i \hat{c}_i^\dagger \hat{c}_i + \sum_{\langle ij \rangle} t_{ij} \hat{c}_i^\dagger \hat{c}_j + \sum_{\langle\langle ij \rangle\rangle} t'_{ij} \hat{c}_i^\dagger \hat{c}_j, \quad (31)$$

where  $E_i \equiv \langle i | \hat{\mathcal{H}} | i \rangle$  is the energy of placing an electron at the lattice site  $i$ , called on-site energy [19].  $t_{ij}$  and  $t'_{ij}$  are the hopping parameters of the NN-sites ( $\langle ij \rangle$ ) and NNN-sites ( $\langle\langle ij \rangle\rangle$ ), respectively, i.e., they are energy terms  $\langle i | \hat{\mathcal{H}} | j \rangle$  for  $i \neq j$  regarding site connections with distances  $|\mathbf{r}_i - \mathbf{r}_j| > |\mathbf{R}|$  greater than the one or more lattice parameters for NN and NNN case, respectively. In summary, for TB models that admit one orbital per site, one has that: (i) if  $i = j$ , then  $t_{ii} = E_i$ , i.e., the on-site energy, and (ii) if  $i \neq j$ , then  $i$  and  $j$  can denote either non-equivalent sites in the unit cell, or equivalent sites separated by lattices vectors.

## 4 Equivalence between First and Second Quantization

In the previous sections, we presented the formulations for the TB model in the first and second quantizations. Generally speaking, the first and second quantizations are not equivalent because they are defined in different vector spaces. While the first is defined in Hilbert space, the second is defined in Fock space. However, it is possible to identify correlations between these spaces [35]. In this section, we shall show the equivalence between the first and second quantization languages within the TB approximation, given some examples of this correspondence in Sect. 6.

### 4.1 From the Second to the First Quantization

Let us now demonstrate that the Hamiltonian in second quantization [see Eq. (30)] leads to the transfer integral matrix [Eq. (11)]. Aiming to this, consider that the creation and annihilation operators at site  $i$  are  $\hat{c}_i^\dagger$  and  $\hat{c}_i$ , respectively. Let us first Fourier-transform these operators, leading them to the momentum space:

$$\hat{c}_i = \frac{1}{\sqrt{N}} \sum_{\mathbf{k}} e^{i\mathbf{k}\cdot\mathbf{r}_i} \hat{c}_{\mathbf{k}}, \quad (32)$$

$$\hat{c}_i^\dagger = \frac{1}{\sqrt{N}} \sum_{\mathbf{k}} e^{-i\mathbf{k}\cdot\mathbf{r}_i} \hat{c}_{\mathbf{k}}^\dagger. \quad (33)$$

The next step is to replace Eqs. (32) and (33) into Eq. (30) for the crystallographic lattice. The resulting equation is simplified by the following identity:

$$\delta'_{\mathbf{kk}} = \frac{1}{N} \sum_i e^{\pm i(\mathbf{k}-\mathbf{k}')\cdot\mathbf{r}_i}. \quad (34)$$

Following these steps, and defining the pseudo-spinor in the Nambu representation, such as

$$|\Psi_{\mathbf{k}}\rangle = (\hat{c}_{\mathbf{k}}^1 \quad \hat{c}_{\mathbf{k}}^2 \quad \dots \quad \hat{c}_{\mathbf{k}}^n)^T, \quad (35)$$

one gets the general demonstration of the equivalence between the first and second quantization formalism, as shown below:

$$\begin{aligned}
 \hat{\mathcal{H}} &= \sum_{ij} t_{ij} \hat{c}_i^\dagger \hat{c}_j \\
 &= \frac{1}{N} \sum_{ij} \sum_{\mathbf{k}} t_{ij} e^{-i\mathbf{k} \cdot \mathbf{r}_i} \hat{c}_{\mathbf{k}}^i \dagger \sum_{\mathbf{k}'} e^{i\mathbf{k}' \cdot \mathbf{r}_j} \hat{c}_{\mathbf{k}'}^j \\
 &= \frac{1}{N} \sum_{ij} \sum_{\mathbf{k}\mathbf{k}'} t_{ij} e^{i\mathbf{k}' \cdot (\mathbf{r}_j - \mathbf{r}_i)} e^{-i(\mathbf{k} - \mathbf{k}') \cdot \mathbf{r}_i} \hat{c}_{\mathbf{k}}^i \dagger \hat{c}_{\mathbf{k}'}^j \\
 &= \frac{1}{N} \sum_i \sum_{\mathbf{k}\mathbf{k}'} \mathcal{H}_{ij}(\mathbf{k}') e^{-i(\mathbf{k} - \mathbf{k}') \cdot \mathbf{r}_i} \hat{c}_{\mathbf{k}}^i \dagger \hat{c}_{\mathbf{k}'}^j \\
 &= \sum_{\mathbf{k}\mathbf{k}'} \delta_{\mathbf{k}\mathbf{k}'} \mathcal{H}_{ij}(\mathbf{k}') \hat{c}_{\mathbf{k}}^i \dagger \hat{c}_{\mathbf{k}'}^j \\
 &= \sum_{\mathbf{k}} \hat{c}_{\mathbf{k}}^i \dagger \mathcal{H}_{ij}(\mathbf{k}) \hat{c}_{\mathbf{k}}^j \\
 &= \sum_{\mathbf{k}} \langle \hat{\Psi}_{\mathbf{k}} | \mathcal{H} | \hat{\Psi}_{\mathbf{k}} \rangle,
 \end{aligned} \tag{36}$$

being used Eq. (13) in the above development. Note that  $\mathcal{H}$  is the same transfer matrix as in Eq. (23).  $\mathcal{H}$

As an example of the path from the second to first quantization, consider a lattice with two non-equivalent sites in the unit cell:  $A$  and  $B$ . The creation and annihilation operators at site localized by  $\mathbf{r}_i$  of the  $A$  ( $B$ ) sublattice are, respectively,  $\hat{a}_i^\dagger$  ( $\hat{b}_i^\dagger$ ) and  $\hat{a}_i$  ( $\hat{b}_i$ ). Thus, according to the steps indicated before, assuming a null on-site energy and taking non-null hoppings just between non-equivalent sites, one has the following direct demonstration:

$$\begin{aligned}
 \hat{\mathcal{H}} &= \sum_{ij} t_{ij} \hat{c}_i^\dagger \hat{c}_j = \frac{1}{N} \sum_{ij} \sum_{\mathbf{k}'} t_{ij} e^{-i\mathbf{k}' \cdot \mathbf{r}_j} \hat{b}_{\mathbf{k}'}^\dagger \sum_{\mathbf{k}} e^{i\mathbf{k} \cdot \mathbf{r}_i} \hat{a}_{\mathbf{k}} \\
 &\quad + \frac{1}{N} \sum_{ij} \sum_{\mathbf{k}} t_{ij} e^{-i\mathbf{k} \cdot \mathbf{r}_i} \hat{a}_{\mathbf{k}}^\dagger \sum_{\mathbf{k}'} e^{i\mathbf{k}' \cdot \mathbf{r}_j} \hat{b}_{\mathbf{k}'} \\
 &= \frac{1}{N} \sum_{ij} \sum_{\mathbf{k}\mathbf{k}'} t_{ij} e^{-i\mathbf{k}' \cdot (\mathbf{r}_j - \mathbf{r}_i)} e^{-i(\mathbf{k}' - \mathbf{k}) \cdot \mathbf{r}_i} \hat{b}_{\mathbf{k}'}^\dagger \hat{a}_{\mathbf{k}} \\
 &\quad + \frac{1}{N} \sum_{ij} \sum_{\mathbf{k}\mathbf{k}'} t_{ij} e^{i\mathbf{k}' \cdot (\mathbf{r}_j - \mathbf{r}_i)} e^{-i(\mathbf{k} - \mathbf{k}') \cdot \mathbf{r}_i} \hat{a}_{\mathbf{k}}^\dagger \hat{b}_{\mathbf{k}'} \\
 &= \frac{1}{N} \sum_i \sum_{\mathbf{k}\mathbf{k}'} \mathcal{H}_{AB}^*(\mathbf{k}') e^{-i(\mathbf{k}' - \mathbf{k}) \cdot \mathbf{r}_i} \hat{b}_{\mathbf{k}'}^\dagger \hat{a}_{\mathbf{k}} \\
 &\quad + \frac{1}{N} \sum_i \sum_{\mathbf{k}\mathbf{k}'} \mathcal{H}_{AB}(\mathbf{k}') e^{-i(\mathbf{k} - \mathbf{k}') \cdot \mathbf{r}_i} \hat{a}_{\mathbf{k}}^\dagger \hat{b}_{\mathbf{k}'} \\
 &= \sum_{\mathbf{k}\mathbf{k}'} \delta_{\mathbf{k}\mathbf{k}'} \left[ \mathcal{H}_{AB}^*(\mathbf{k}') \hat{b}_{\mathbf{k}'}^\dagger \hat{a}_{\mathbf{k}} + \mathcal{H}_{AB}(\mathbf{k}') \hat{a}_{\mathbf{k}}^\dagger \hat{b}_{\mathbf{k}'} \right] \\
 &= \sum_{\mathbf{k}} \left[ \mathcal{H}_{AB}^*(\mathbf{k}) \hat{b}_{\mathbf{k}}^\dagger \hat{a}_{\mathbf{k}} + \mathcal{H}_{AB}(\mathbf{k}) \hat{a}_{\mathbf{k}}^\dagger \hat{b}_{\mathbf{k}} \right] \\
 &= \sum_{\mathbf{k}} \left( \begin{pmatrix} \hat{a}_{\mathbf{k}}^\dagger & \hat{b}_{\mathbf{k}}^\dagger \end{pmatrix} \begin{pmatrix} 0 & \mathcal{H}_{AB}(\mathbf{k}) \\ \mathcal{H}_{AB}^*(\mathbf{k}) & 0 \end{pmatrix} \begin{pmatrix} \hat{a}_{\mathbf{k}} \\ \hat{b}_{\mathbf{k}} \end{pmatrix} \right) \\
 &= \sum_{\mathbf{k}} \langle \hat{\Psi}_{\mathbf{k}} | \mathcal{H} | \hat{\Psi}_{\mathbf{k}} \rangle,
 \end{aligned} \tag{37}$$

where  $\mathcal{H}$  is the TB Hamiltonian in the first quantization (transfer integral matrix) and  $\hat{\mathcal{H}}$  is the corresponding TB Hamiltonian in the second quantization.

In comparison with the LCAO, the overlap matrix in the second quantization language is supposed to always be equal the identity matrix. This restriction does not greatly reduce the generality of the method in second quantization, because the TB model is generally used when we consider, by approximation, that there is no overlap between the atomic functions of the sites. It is so true that the complete set of Bloch functions can be written as linear combinations of the Wannier functions, which are orthogonal at different sites (or with different band indices) unlike TB atomic functions of LCAO. In fact, the LCAO is a variational method that does not guarantee a complete basis of the Hilbert space, making it impossible to accurately map the first and second quantizations. Such mapping is only possible via Wannier functions that form a complete orthogonal set, such that offer an alternative basis for an exact description of the independent electron levels in a crystal potential [15].

## 4.2 From the First to the Second Quantization

Starting from the resulting expression in Eq. (36) within the first quantization language, we are able to obtain the representation of the Hamiltonian in the second quantization simply following the opposite path of this derivation. Therefore, after finding the transfer integral matrix by the first quantization TB model, one acts  $\langle \hat{\Psi}_{\mathbf{k}} |$  and  $| \hat{\Psi}_{\mathbf{k}} \rangle$  to the left and to the right of  $\mathcal{H}$ , respectively. Once done, we add a sum in  $\mathbf{k}'$  with the Kronecker delta  $\delta_{\mathbf{k}\mathbf{k}'}$  [see Eq. (34)]. This step does not change the Hamiltonian and ensures that we can identify the Fourier transforms of creation and annihilation operators [see Eqs. (32)–(33)]. In summary, these steps lead to

$$\begin{aligned}
 \hat{\mathcal{H}} &= \sum_{\mathbf{k}} \langle \hat{\Psi}_{\mathbf{k}} | \mathcal{H} | \hat{\Psi}_{\mathbf{k}} \rangle \\
 &= \sum_{\mathbf{k}} \hat{c}_{\mathbf{k}}^i \dagger \mathcal{H}_{ij}(\mathbf{k}) \hat{c}_{\mathbf{k}}^j \\
 &= \sum_{\mathbf{k}\mathbf{k}'} \delta_{\mathbf{k}\mathbf{k}'} \hat{c}_{\mathbf{k}}^i \dagger \mathcal{H}_{ij}(\mathbf{k}') \hat{c}_{\mathbf{k}'}^j \\
 &= \sum_{\mathbf{k}\mathbf{k}'} \frac{1}{N} \sum_i e^{-i(\mathbf{k} - \mathbf{k}') \cdot \mathbf{r}_i} \hat{c}_{\mathbf{k}}^i \dagger \mathcal{H}_{ij}(\mathbf{k}') \hat{c}_{\mathbf{k}'}^j \\
 &= \sum_{ij} \sum_{\mathbf{k}\mathbf{k}'} \frac{1}{N} e^{-i(\mathbf{k} - \mathbf{k}') \cdot \mathbf{r}_i} \hat{c}_{\mathbf{k}}^i \dagger t_{ij} e^{i\mathbf{k}' \cdot (\mathbf{r}_j - \mathbf{r}_i)} \hat{c}_{\mathbf{k}'}^j \\
 &= \sum_{ij} t_{ij} \frac{1}{\sqrt{N}} \sum_{\mathbf{k}} e^{-i\mathbf{k} \cdot \mathbf{r}_i} \hat{c}_{\mathbf{k}}^i \dagger \frac{1}{\sqrt{N}} \sum_{\mathbf{k}'} e^{i\mathbf{k}' \cdot \mathbf{r}_j} \hat{c}_{\mathbf{k}'}^j \\
 &= \sum_{ij} t_{ij} \hat{c}_i^\dagger \hat{c}_j,
 \end{aligned} \tag{38}$$

where  $\mathcal{H}_{ij}$  are the transfer matrix elements, as represented in Eq. (11).

To exemplify the equivalence between the first and second quantization languages of the TB model for the calculation of energy spectrum, in Sect. 6 we compute the energy levels with the both formalisms for different one- and two-dimensional lattices with: one, two and three non-equivalent sites within the unit cell. Before that, in Sect. 5 we systematize the steps to obtain the energy spectrum starting from a real lattice.

## 5 Band Structure Calculation

In the previous sections, we described the basic concepts of the TB method in the first and second quantization. Let us now present the steps for applying the method to the calculation of band structures of crystals.

### 5.1 Analysis of the Crystal Structure and the Bravais Lattice

One starts by identifying the lattice structure of the system. That may not be necessarily the actual crystal structure of the material, since depending on the level of precision and the energy range which one wants to describe, one can restrict the relevant orbitals to regard in the model. It allows in certain circumstances to neglect the hopping between some atomic sites, specially NNN connections. Then, an association of the structure with a specific Bravais lattice is made (or with two or more Bravais sublattices). Taking the crystal structure and its unit cell containing information about the primitive vectors  $\mathbf{a}_1$ ,  $\mathbf{a}_2$  and  $\mathbf{a}_3$ , the coordinates of the atomic sites that form the unit cell base are then defined.

### 5.2 Analysis of the Reciprocal Space and the First Brillouin Zone

The energy eigenvalues of the total Hamiltonian are periodic functions in the reciprocal space, which can be very neatly described within the first Brillouin zone, which is the Wigner–Seitz cell in the reciprocal space. Thus, the reciprocal lattice and the first Brillouin zone are built from the Bravais lattice determined in the previous item. The reciprocal lattice, defined by the primitive vectors  $\mathbf{b}_1$ ,  $\mathbf{b}_2$  and  $\mathbf{b}_3$ , is easily obtained from the primitive vectors of the Bravais lattice ( $\mathbf{a}_1$ ,  $\mathbf{a}_2$  and  $\mathbf{a}_3$ ) by the relations:

$$\mathbf{b}_1 = 2\pi \frac{\mathbf{a}_2 \times \mathbf{a}_3}{\mathbf{a}_1 \cdot \mathbf{a}_2 \times \mathbf{a}_3}, \quad (39)$$

$$\mathbf{b}_2 = 2\pi \frac{\mathbf{a}_3 \times \mathbf{a}_1}{\mathbf{a}_1 \cdot \mathbf{a}_2 \times \mathbf{a}_3}, \quad (40)$$

$$\mathbf{b}_3 = 2\pi \frac{\mathbf{a}_1 \times \mathbf{a}_2}{\mathbf{a}_1 \cdot \mathbf{a}_2 \times \mathbf{a}_3}, \quad (41)$$

where each of the vectors defined by Eqs. (39)–(41) is perpendicular to two axes of the Bravais lattice, obeying therefore the following property:  $\mathbf{b}_i \cdot \mathbf{a}_j = 2\pi\delta_{ij}$ , being  $\delta_{ij}$  the Kronecker delta [23].

### 5.3 Determination of Transfer and Overlap Matrices

At this point, the calculation of the transfer integral matrix elements is done using the first or second quantization formalism. On the other hand, the overlap matrix elements are usually computed via the first quantization, since in the second quantization the overlap matrix is always the identity matrix. The model used must be the one that provides the energy bands that best fit the results provided by the first principle calculations, without neglecting the essence of the approximation, which is the assumption of TB model itself.

Throughout the paper, we only consider interactions between NN sites. Due to the terms  $\sum_{\mathbf{k}} \hat{c}_{\mathbf{k}}^i \hat{c}_{\mathbf{k}}^{i\dagger} \mathcal{H}_{ij}(\mathbf{k}) \hat{c}_{\mathbf{k}}^j$  in Eqs. (36) and (38), each  $\mathcal{H}_{ij}$  element is calculated admitting that the electron is annihilated (created) at sites of  $j$  ( $i$ ) type. In addition, the system coordinate origin for the  $\mathcal{H}_{ij}$  computing is on a site  $i$  and one takes  $j$  to run over the NN sites assumed in the TB model for each investigated case.

### 5.4 Energy Eigenvalues

Using the transfer integral and overlap matrices, the energy eigenvalues are obtained from the secular equation, Eq. (22).

### 5.5 Density of States

The evaluation of the density of states (DOS) is then performed by a superposition of individual energy states which we broaden using a Gaussian function

$$f(E) = e^{-(E-E_0)^2/\gamma^2}, \quad (42)$$

with a broadening factor  $\gamma$  smaller than the energy levels separations.  $\gamma = 0.05$  eV was assumed for all figures from here onward, unless otherwise stated [24].

## 6 Application Examples

Let us now use the procedure described in the previous sections to determine the energy bands of five crystal lattices, namely (Fig. 1(a) and (b)) linear chain, (Fig. 1(c) and (d)) square lattice, (Fig. 1(e)) graphene, (Fig. 1(f)) brick lattice and (Fig. 1(g))  $\tau_3$ -lattice. The band structure of each crystal lattice is obtained by means of the TB method in the first and second quantization. We consider only interactions between

NN sites taking only one atomic orbital per site in all the following calculations. For linear chain and square lattices, two different situations are analyzed: the case of one and two sites per unit cell.

## 6.1 Linear Chain in the First Quantization

Let us start with the simplest case, that is, the linear chain containing only one site per unit cell, as shown in Fig. 1(a). The primitive vectors of the real lattice and the reciprocal lattice are, respectively,  $\mathbf{a}_1 = (a, 0, 0)$  and  $\mathbf{b}_1 = (2\pi/a, 0, 0)$ . The first Brillouin zone is specified by  $-\pi/a \leq k \leq +\pi/a$ , as shown in Fig. 2(a). The Bloch function is then written as

$$\Phi_j(\mathbf{r}, \mathbf{k}) = \frac{1}{\sqrt{N}} \sum_{\mathbf{R}} e^{i\mathbf{k} \cdot \mathbf{R}} \varphi_j(\mathbf{r} - \mathbf{R}), \quad (43)$$

so that the transfer integral matrix is

$$\mathcal{H} = \frac{1}{N} \left( N\epsilon_0 + Nt \sum_{n=1}^2 e^{i\mathbf{k} \cdot \mathbf{d}_n} \right) = \epsilon_0 + 2t \cos(ka), \quad (44)$$

where  $\mathbf{d}_n$  are the NN sites:  $\mathbf{d}_1 = (a, 0)$  and  $\mathbf{d}_2 = (-a, 0)$ . Likewise, the overlap matrix is given by

$$\mathcal{S} = \frac{1}{N} \left( N + Ns \sum_{n=1}^2 e^{i\mathbf{k} \cdot \mathbf{d}_n} \right) = 1 + 2s \cos(ka). \quad (45)$$

Thus, the solution of Eq. (22) for the linear chain containing only one site in the unit cell is immediate and reads

$$E(\mathbf{k}) = \frac{\epsilon_0 + 2t \cos(ka)}{1 + 2s \cos(ka)}. \quad (46)$$

Figure 3(a) depicts the energy spectrum of a linear chain with one site per unit cell. Solid and dashed lines correspond to  $s = 0$  and  $s \neq 0$  cases, respectively. The plot is shown in an interval comprising a unit cell at positive values of  $k$ ,  $0 \leq k \leq 2\pi/a$ , to facilitate comparison with the other investigated cases here, whose energy spectra are plotted along the high symmetry points in the region of positive values of  $k$ . Notice that the nonzero overlap parameter (i.e.,  $s \neq 0$ ) causes a symmetry breaking with respect to  $E = 0$ . The region below (above) the zero level,  $E = 0$ , is compressed (extended) in relation to the energy axis, having its minimum (maximum) value in a smaller (larger) modulus than the case without overlap.

With two non-equivalent sites,  $A$  and  $B$ , per unit cell in the linear chain, as shown in Fig. 1(b), the primitive vectors of the real and reciprocal lattices are, respectively,  $\mathbf{a}_1 = (2a, 0, 0)$  and  $\mathbf{b}_1 = (\pi/a, 0, 0)$ . Therefore, the first Brillouin zone, shown in Fig. 2(b), is specified by  $-\pi/2a \leq k \leq +\pi/2a$ , and the Bloch function, now consisting of  $A$  and  $B$  sites, is written as

$$\Phi_j(\mathbf{r}, \mathbf{k}) = \frac{1}{\sqrt{N}} \sum_{\mathbf{R}_\alpha} e^{i\mathbf{k} \cdot \mathbf{R}_\alpha} \varphi_j(\mathbf{r} - \mathbf{R}_\alpha), \quad \alpha = (A, B). \quad (47)$$

Once there are two atomic orbitals in the unit cell, the transfer integral and overlap matrices,  $\mathcal{H}$  and  $\mathcal{S}$ , are both  $2 \times 2$  matrices and given by

$$\mathcal{H} = \begin{pmatrix} \mathcal{H}_{AA} & \mathcal{H}_{AB} \\ \mathcal{H}_{BA} & \mathcal{H}_{BB} \end{pmatrix}, \quad \mathcal{S} = \begin{pmatrix} \mathcal{S}_{AA} & \mathcal{S}_{AB} \\ \mathcal{S}_{BA} & \mathcal{S}_{BB} \end{pmatrix}. \quad (48)$$

In this case, the NN sites are  $\mathbf{d}_1 = (a, 0)$  and  $\mathbf{d}_2 = (-a, 0)$ . Thus,  $\mathcal{H}_{AA} = \epsilon_A$ ,  $\mathcal{H}_{BB} = \epsilon_B$  and  $\mathcal{H}_{AB} = \mathcal{H}_{BA} = 2t \cos(ka)$ . Likewise, we have  $\mathcal{S}_{AA} = \mathcal{S}_{BB} = 1$  and  $\mathcal{S}_{AB} = \mathcal{S}_{BA} = 2s \cos(ka)$ . Thus, the secular equation is given by

$$\det \begin{bmatrix} \epsilon_A - E_\pm(\mathbf{k}) & 2[t - sE_\pm(\mathbf{k})] \cos(ka) \\ 2[t - sE_\pm(\mathbf{k})] \cos(ka) & \epsilon_B - E_\pm(\mathbf{k}) \end{bmatrix} = 0. \quad (49)$$

If sites  $A$  and  $B$  are the same constituents, one has  $\epsilon_A = \epsilon_B = \epsilon_0$ , so that the resulting solution is

$$E_\pm(\mathbf{k}) = \frac{\epsilon_0 \pm 2t \cos(ka)}{1 \pm 2s \cos(ka)}, \quad (50)$$

where  $E_+(\mathbf{k})$  and  $E_-(\mathbf{k})$  are degenerate at  $ka = \pm\pi/2$  and are called bonding and anti-bonding energy bands [16], respectively. Figure 3(b) shows the linear chain dispersion relation with two sites per unit cell, where solid and dashed lines corresponding to null ( $s = 0$ ) and non-null ( $s \neq 0$ ) overlap cases, and the  $k$  interval ( $0 \leq k \leq 2\pi/a$ ) is taken the same as in Fig. 3(a) to better comparison. Similarly to the case of one site per unit cell (Fig. 3(a)), the overlap breaks the energy symmetry with respect to  $E = 0$  axis. Due to the existence of two non-equivalent sites, one obtains two energy bands  $E_+$  (red lines) and  $E_-$  (blue lines), instead of only one as in the case of a single site, that are symmetrical in energy and momentum and which intersect each other at the zero energy level.

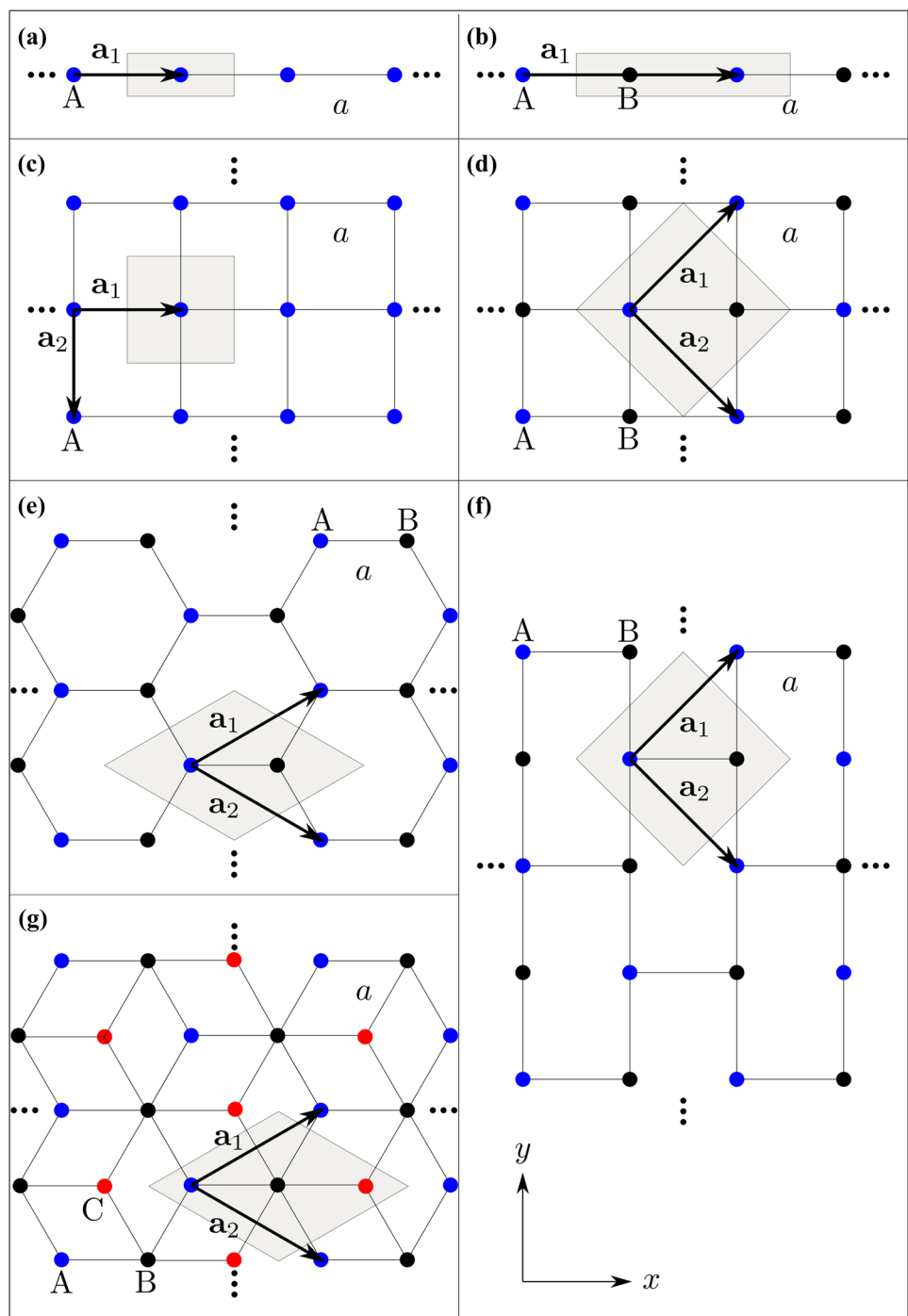
## 6.2 Linear Chain in Second Quantization

In second quantization, the Hamiltonian for a linear chain with one site per unit cell can be written as

$$\hat{\mathcal{H}} = \sum_i \epsilon_0 \hat{c}_i^\dagger \hat{c}_i + \sum_i t \left( \hat{c}_i^\dagger c_{i+1} + \hat{c}_{i+1}^\dagger c_i \right), \quad (51)$$

where the creation and annihilation operators act upon a basis of orthogonal states [26],  $\epsilon_0 = t_{i,i}$  represents the energy of an electron at site  $i$ , and  $t = t_{i,i+1}$  denotes the hopping energy associated with the sites  $i$  to  $i+1$ .  $\hat{c}_i$  and  $\hat{c}_i^\dagger$  can be expressed in the momentum space as

**Fig. 1** Crystal structures studied in this paper: linear chain with (a) one and (b) two sites in the unit cell, square lattice with (c) one and (d) two sites in the unit cell, (e) graphene, known as honeycomb lattice, (f) brick lattice, a square lattice with some neglected hopping parameters being topologically equivalent to graphene, and (g)  $\tau_3$ -lattice, whose difference from graphene lies in the fact that it has an atom in the center of each hexagon. In all panels, the lattice parameter is  $a$ , the primitive vectors are denoted by  $\mathbf{a}_p$  ( $p = 1, 2$ ), and the unit cell is highlighted in gray



$$\hat{c}_i = \frac{1}{\sqrt{N}} \sum_{\mathbf{k}} e^{i\mathbf{k} \cdot \mathbf{r}_i} \hat{c}_{\mathbf{k}}, \quad \hat{c}_i^\dagger = \frac{1}{\sqrt{N}} \sum_{\mathbf{k}} e^{-i\mathbf{k} \cdot \mathbf{r}_i} \hat{c}_{\mathbf{k}}^\dagger, \quad (52)$$

resulting, by replacing into Eq. (51), in

$$\begin{aligned} \hat{\mathcal{H}} &= \sum_{\mathbf{k}} \hat{c}_{\mathbf{k}}^\dagger \frac{1}{N} \left( N\epsilon_0 + Nt \sum_{n=1}^2 e^{i\mathbf{k} \cdot \mathbf{d}_n} \right) \hat{c}_{\mathbf{k}} \\ &= \sum_{\mathbf{k}} [\hat{c}_{\mathbf{k}}^\dagger \epsilon_0 \hat{c}_{\mathbf{k}} + \hat{c}_{\mathbf{k}}^\dagger t f(\mathbf{k}) \hat{c}_{\mathbf{k}}], \end{aligned} \quad (53)$$

where  $f(\mathbf{k}) = \sum_{n=1}^2 e^{i\mathbf{k} \cdot \mathbf{d}_n}$  is called the geometric structure factor [15]. Equation (53) can be rewritten as

$$\hat{\mathcal{H}} = \sum_{\mathbf{k}} \hat{c}_{\mathbf{k}}^\dagger [\epsilon_0 + t f(\mathbf{k})] \hat{c}_{\mathbf{k}} = \sum_{\mathbf{k}} \hat{c}_{\mathbf{k}}^\dagger \mathcal{H} \hat{c}_{\mathbf{k}}.$$

$\mathcal{H}$ , in turn, is the transfer integral matrix (see Eq. (44)) and directly gives us the dispersion relation (see Fig. 3(a)):

$$E(\mathbf{k}) = \epsilon_0 + 2t \cos(ka). \quad (54)$$

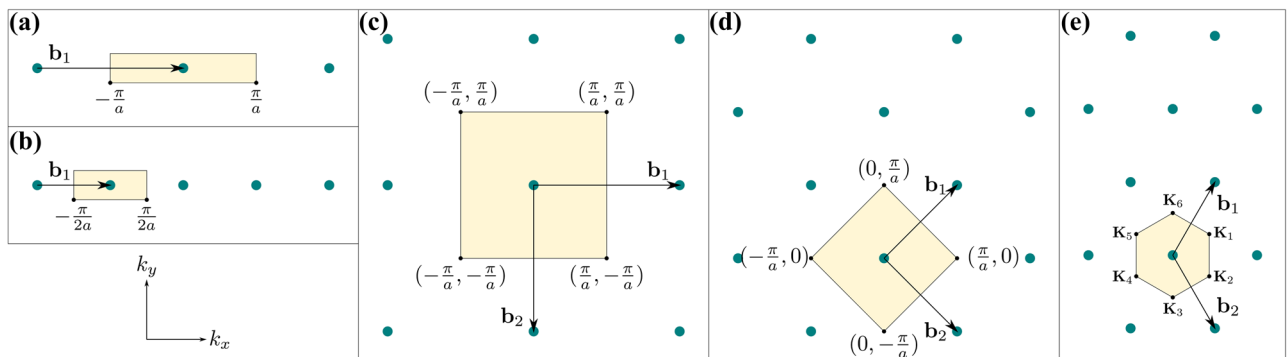


**Fig. 2** Reciprocal lattices of the investigated crystal structures of Fig. 1: (a) and (b) linear chain with one and two sites in the unit cell, respectively, (c) square lattice with one site in the unit cell, (d) square lattice with two sites in the unit cell and brick lattice, and (e) graphene and  $\tau_3$ -lattice. Yellow shaded region highlights the first Brillouin zone, and the primitive vectors are denoted

by  $\mathbf{b}_p$  ( $p = 1, 2$ ). For graphene and  $\tau_3$ -lattice, it is a hexagon with vertices  $\mathbf{K}_1 = [2\pi/(3a), 2\pi/(3\sqrt{3}a)]$ ,  $\mathbf{K}_2 = [2\pi/(3a), -2\pi/(3\sqrt{3}a)]$ ,  $\mathbf{K}_3 = [0, -4\pi/(3\sqrt{3}a)]$ ,  $\mathbf{K}_4 = [-2\pi/(3a), -2\pi/(3\sqrt{3}a)]$ ,  $\mathbf{K}_5 = [-2\pi/(3a), 2\pi/(3\sqrt{3}a)]$  and  $\mathbf{K}_6 = [0, 4\pi/(3\sqrt{3}a)]$ . Of these six points, only two are not equivalent, which are called Dirac points in the graphene spectrum and are triply degenerate points in the  $\tau_3$ -lattice spectrum

For the linear chain with two sites in the unit cell, the Hamiltonian reads

$$\hat{\mathcal{H}} = \sum_i \epsilon_A a_i^\dagger a_i + \sum_j \epsilon_B b_j^\dagger b_j + \sum_{i,j} t(a_i^\dagger b_j + b_j^\dagger a_i), \quad (55)$$

where  $\epsilon_{A(B)}$  represents the on-site energy of an electron at sublattice A (B) (see Fig. 1(b)), and  $t$  is the NN hopping parameter connecting the sublattices A and B. Using Eqs. (32)–(33) and taking  $\epsilon_A = \epsilon_B = \epsilon_0$ , the Hamiltonian (55) can be simplified to

$$\hat{\mathcal{H}} = \sum_{\mathbf{k}} [a_{\mathbf{k}}^\dagger \epsilon_0 a_{\mathbf{k}} + b_{\mathbf{k}}^\dagger \epsilon_0 b_{\mathbf{k}} + a_{\mathbf{k}}^\dagger t f(\mathbf{k}) b_{\mathbf{k}} + b_{\mathbf{k}}^\dagger t f(\mathbf{k})^* a_{\mathbf{k}}], \quad (56)$$

which can be rewritten as

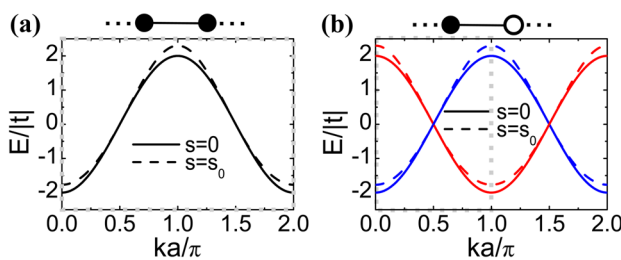


**Fig. 3** Energy spectrum of a linear chain with (a) one and (b) two sites per unit cell. Solid and dashed lines correspond to the cases with zero overlap ( $s = 0$ ) and non-null overlap ( $s \neq 0$ ), respectively. Blue and red lines in panel (b) denote the energy bands  $E_+$  and  $E_-$ , respectively. Inspired by graphene case, for comparison purposes, we adopted  $s_0 = 0.065$  and  $t = -2.74$  eV [25]. The first Brillouin zone is highlighted by gray dashed line

$$\hat{\mathcal{H}} = \sum_{\mathbf{k}} [a_{\mathbf{k}}^\dagger b_{\mathbf{k}}^\dagger] \begin{bmatrix} \epsilon_0 & t f(\mathbf{k}) \\ t f(\mathbf{k})^* & \epsilon_0 \end{bmatrix} \begin{bmatrix} a_{\mathbf{k}} \\ b_{\mathbf{k}} \end{bmatrix} = \sum_{\mathbf{k}} \langle \Psi_{\mathbf{k}} | \mathcal{H} | \Psi_{\mathbf{k}} \rangle. \quad (57)$$

Diagonalizing the matrix form of the Hamiltonian of Eq. (57), we obtain the energy bands (see Fig. 3(b)), given by

$$E_{\pm}(\mathbf{k}) = \epsilon_0 \pm 2t \cos(ka). \quad (58)$$

### 6.3 Square Lattice in the First Quantization

Now, we present a similar calculation of how to obtain the energy bands for the square lattice with one and two atoms per unit cell. The former can be obtained by expanding the linear chain in two dimensions, as shown in Fig. 1(c). Its primitive vectors of the real and reciprocal lattices are  $\mathbf{a}_1 = (a, 0, 0)$  and  $\mathbf{a}_2 = (0, -a, 0)$ , and  $\mathbf{b}_1 = (2\pi/a, 0, 0)$  and  $\mathbf{b}_2 = (0, -2\pi/a, 0)$ , respectively. The first Brillouin zone, in turn, is specified by  $-\pi/a \leq k_x \leq +\pi/a$  and  $-\pi/a \leq k_y \leq +\pi/a$ , as depicted in Fig. 2(c). The distances between NN sites are:  $\mathbf{d}_1 = (a, 0)$ ,  $\mathbf{d}_2 = (-a, 0)$ ,  $\mathbf{d}_3 = (0, a)$ ,  $\mathbf{d}_4 = (0, -a)$ . Thus, the transfer integral matrix can be calculated as

$$\begin{aligned} \mathcal{H} &= \frac{1}{N} \left( N\epsilon_0 + Nt \sum_{n=1}^4 e^{i\mathbf{k} \cdot \mathbf{d}_n} \right) \\ &= \epsilon_0 + 2t[\cos(k_x a) + \cos(k_y a)], \end{aligned} \quad (59)$$

and likewise, the overlap matrix is written as

$$\begin{aligned} \mathcal{S} &= \frac{1}{N} \left( N + N_s \sum_{n=1}^4 e^{i\mathbf{k} \cdot \mathbf{d}_n} \right) \\ &= 1 + 2s[\cos(k_x a) + \cos(k_y a)]. \end{aligned} \quad (60)$$

Using  $\mathcal{H}$  and  $\mathcal{S}$  of Eqs. (59) and (60) into the secular Eq. (22), one obtains the energy band for the square lattice containing only one site in the unit cell, such as

$$E(\mathbf{k}) = \frac{\epsilon_0 + 2t[\cos(k_x a) + \cos(k_y a)]}{1 + 2s[\cos(k_x a) + \cos(k_y a)]}. \quad (61)$$

Figure 4(a) shows the energy spectrum by taking the overlap parameter  $s = 0$  (solid line) and  $s \neq 0$  (dashed line), along the high symmetry points  $\Gamma = (0, 0)$ ,  $\mathbf{X} = (\pi/a, 0)$  and  $\mathbf{M} = (\pi/a, \pi/a)$  as labeled in right contour plot panel, and the DOS for the square lattice with one site per unit cell. Right panels in Fig. 4(a) present contour plots of the bands for  $s = 0$  and  $s \neq 0$  cases, exhibiting an energy shift to high-energy values, especially on the borders of the  $\Gamma - \mathbf{X}$  and  $\mathbf{M} - \Gamma$  directions, as also clearly seen in the left panel. Notice a symmetry breaking in the energy band and, consequently, in the DOS, with respect to zero energy when one regards a nonzero overlap contribution, similarly to the one observed in Fig. 3 for a non-null overlap energy in the linear chain. This electron–hole symmetry breaking caused by the overlap energy effect leads to a DOS imbalance around the large peak in  $E = 0$ .

Let us now consider the case of two,  $A$  and  $B$ , non-equivalent sites per unit cell for the square lattice, as illustrated in Fig. 1(d). The primitive real and reciprocal vectors are  $\mathbf{a}_1 = (a, a, 0)$  and  $\mathbf{a}_2 = (a, -a, 0)$ , and  $\mathbf{b}_1 = (\pi/a, \pi/a, 0)$  and  $\mathbf{b}_2 = (\pi/a, -\pi/a, 0)$ , respectively, and the distances between the NN atomic sites are the same as the previous case:  $\mathbf{d}_1 = (a, 0)$ ,  $\mathbf{d}_2 = (-a, 0)$ ,  $\mathbf{d}_3 = (0, a)$ ,  $\mathbf{d}_4 = (0, -a)$ . The first Brillouin zone is defined in the following  $k$ -interval:  $k_{x,y} \in [-\pi/a, \pi/a]$ , as shown in Fig. 2(d). Thus, taking  $\epsilon_A = \epsilon_B = \epsilon_0$ , the resulting secular Eq. (23) is

$$\det \begin{bmatrix} \Pi & \Delta \\ \Delta & \Pi \end{bmatrix} = 0, \quad (62)$$

where  $\Delta = 2[t - sE_{\pm}(\mathbf{k})][\cos(k_x a) + \cos(k_y a)]$  and  $\Pi = \epsilon_0 - E_{\pm}(\mathbf{k})$ , leading to the following solution:

$$E_{\pm}(\mathbf{k}) = \frac{\epsilon_0 \pm 2t[\cos(k_x a) + \cos(k_y a)]}{1 \pm 2s[\cos(k_x a) + \cos(k_y a)]}. \quad (63)$$

Since the lattice has two atoms per unit cell, similarly to a two-level system, one obtains two bands  $E_+$  and  $E_-$ , where + and – signs in Eq. (63) denote electron and hole bands. The energy spectrum and DOS are shown in Fig. 4(b), where red and blue solid (dashed) lines correspond to  $s = 0$  ( $s \neq 0$ )

case for  $E_+$  and  $E_-$  bands, respectively. The  $k$ -space direction is along the high symmetry points  $\Gamma = (0, 0)$ ,  $\mathbf{M} = (\pi/a, 0)$ ,  $\mathbf{Y} = (0, \pi/a)$ , as indicated on the corresponding contour plot panel by the triangle along  $\Gamma - \mathbf{M} - \mathbf{Y} - \Gamma$ . As already discussed for the linear chain and square lattice with one site per unit cell,  $s \neq 0$  parameter shifts non-equivalently the energy spectrum along the whole Brillouin zone breaking the electron–hole symmetry and causes an unbalance in the area under the DOS curve for positive and negative energy values. By the chosen  $k$ -space direction, the  $\mathbf{M} - \Gamma$ -path has a flat band with both conduction and valence bands touching themselves at  $E = 0$ . In order to analyze the emergence of the second band in comparison with the square lattice case with one atom per unit cell, we depict in Fig. 5(a) the energy spectrum along the high symmetry points of square lattice with one site (see inset triangles in Figs. 4(a) and 5(a)). It can be seen that the consideration of two non-equivalent sites brings up a second band (red line,  $E_-$ ) obeying the electron–hole symmetry with respect to the one site already existing band, i.e.,  $E_+ = -E_-$ .

#### 6.4 Square Lattice in the Second Quantization

The Hamiltonian in the second quantization for the square lattice with one site per unit cell can be written as

$$\hat{\mathcal{H}} = \sum_i \epsilon_0 \hat{c}_i^\dagger \hat{c}_i + \sum_{i,j} t \hat{c}_i^\dagger \hat{c}_j. \quad (64)$$

For square lattice regarding only NN sites, each site  $i$  is connected to four other sites  $j$  (see Fig. 1(c)) with hopping energy  $t$ . The first term in Eq. (64) is associated with the on-site. Using Eqs. (32)–(33), the Hamiltonian (64) can be simplified to

$$\hat{\mathcal{H}} = \sum_{\mathbf{k}} [\hat{c}_{\mathbf{k}}^\dagger \epsilon_0 \hat{c}_{\mathbf{k}} + \hat{c}_{\mathbf{k}}^\dagger t f(\mathbf{k}) \hat{c}_{\mathbf{k}}], \quad (65)$$

with the geometric structure factor being  $f(\mathbf{k}) = \sum_{n=1}^4 e^{i\mathbf{k} \cdot \mathbf{d}_n}$ . Equation (65) can be rewritten as

$$\hat{\mathcal{H}} = \sum_{\mathbf{k}} \hat{c}_{\mathbf{k}}^\dagger \mathcal{H} \hat{c}_{\mathbf{k}}, \quad (66)$$

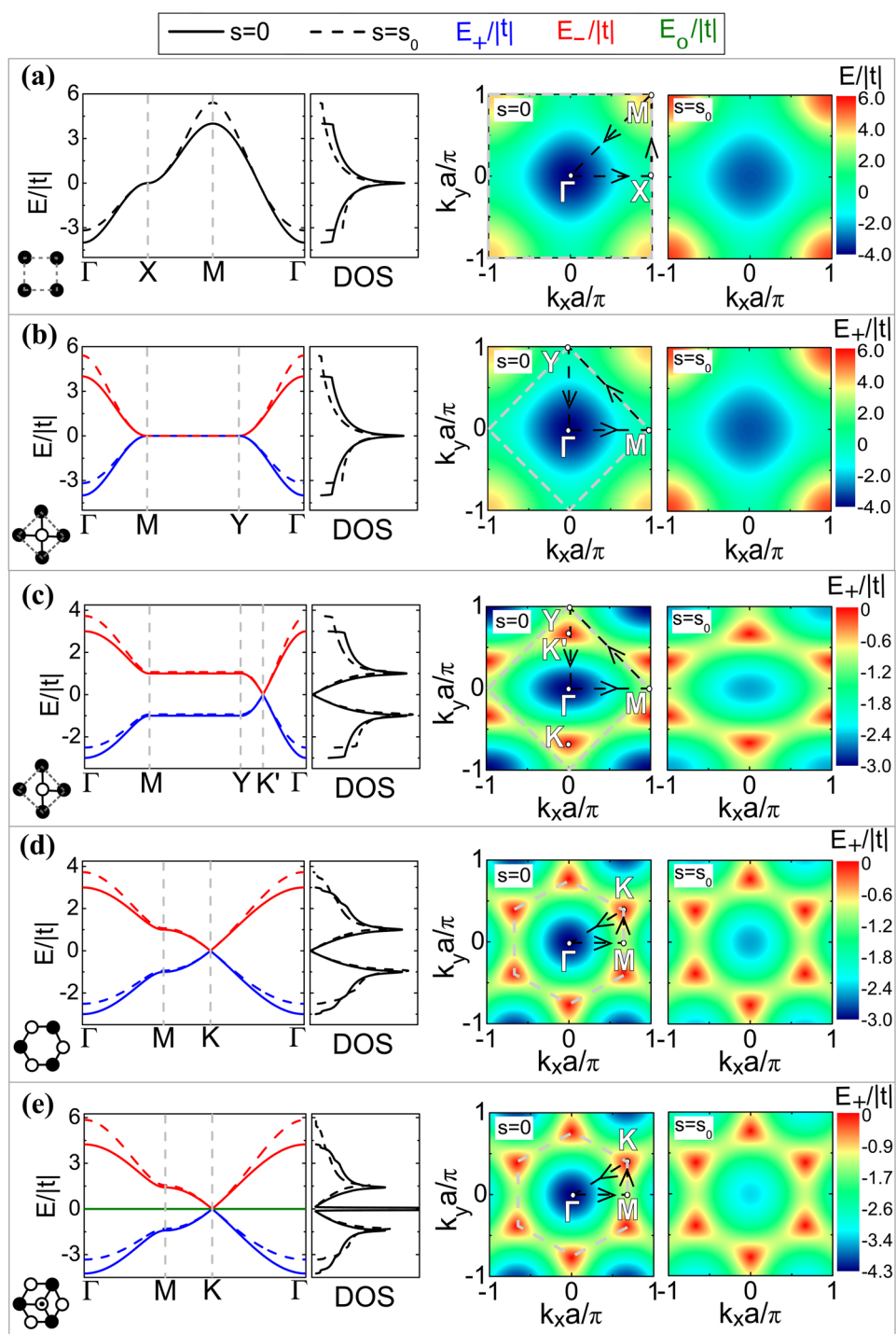
where it directly gives us the dispersion relation (see Fig. 4(a)):

$$E(\mathbf{k}) = \epsilon_0 + 2t[\cos(k_x a) + \cos(k_y a)]. \quad (67)$$

In the same way, for two-site square lattice, the Hamiltonian in the second quantization formalism reads

$$\hat{\mathcal{H}} = \sum_i \epsilon_A a_i^\dagger a_i + \sum_j \epsilon_B b_j^\dagger b_j + \sum_{i,j} t (a_i^\dagger b_j + b_j^\dagger a_i), \quad (68)$$

**Fig. 4** Energy spectrum and DOS for: square lattice with (a) one and (b) two atoms per unit cell, (c) brick lattice, (d) graphene and (e)  $\tau_3$ -lattice. Solid and dashed lines correspond to the cases with zero overlap ( $s = 0$ ) and non-null overlap ( $s \neq 0$ ), respectively. Blue, red and green lines denote the energy bands  $E_+$ ,  $E_-$  and  $E_0$ , respectively. Inspired by graphene case, for comparison purposes, we adopted  $s_0 = 0.065$  and  $t = -2.74$  eV. [25] Right panels correspond to the contour plots of the conduction bands for  $s = 0$  and  $s \neq 0$ , emphasizing the first Brillouin zone, highlighted by gray dashed line, the high symmetry points and the paths taken for the energy plots in  $k$ -space



where  $\epsilon_{A,B}$  and  $t$  have the same definitions as in Eq. (59). Again, using Eqs. (32)–(33) and taking  $\epsilon_A = \epsilon_B = \epsilon_0$ , the Hamiltonian (68) can be simplified to

$$\hat{\mathcal{H}} = \sum_{\mathbf{k}} \langle \Psi_{\mathbf{k}} | \mathcal{H} | \Psi_{\mathbf{k}} \rangle. \quad (69)$$

Diagonalizing Eq. (69), one gets the energy bands  $\mathcal{H}$  as depicted in Figs. 4(b) and 5(a) and given by

$$E_{\pm}(\mathbf{k}) = \epsilon_0 \pm 2t[\cos(k_x a) + \cos(k_y a)]. \quad (70)$$

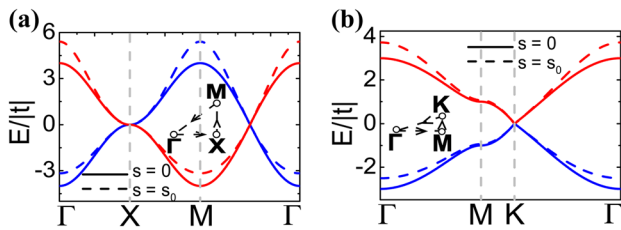


**Fig. 5** Energy spectrum of (a) the square lattice with two sites per unit cell and (b) the brick lattice. The assumed  $k$ -space paths in (a) and (b) are illustrated in the inset of each panel, being similar to the ones for the square lattice with one site per unit cell and graphene, respectively, as shown in Fig. 4(a) and (e). It was adopted the same parameters as in Fig. 4

## 6.5 Brick Lattice in the First Quantization

Let us now describe a square lattice topologically similar to graphene that is defined with some hopping parameters being neglected, called brick lattice [27, 28]. As we shall present, the energy spectra of both graphene and brick lattices are similar due to the equivalent topological lattice mapping between them within the TB model with interactions only between NN sites. Models for more general honeycomb crystal structures were investigated in Refs. [29] and [30]. To illustrate more examples of such similar lattice mapping, a square lattice model topologically equivalent to phosphorene (a puckered monolayer black phosphorus lattice with a highly anisotropic band structure) was investigated in Ref. [31], where different NN hopping values were assumed to simulate the phosphorene lattice anisotropy. Notice, by assuming three nonvanishing NN hopping parameters in Fig. 1(d), that the brick lattice shown in Fig. 1(f) is topologically equivalent to the crystal structure of graphene shown in Fig. 1(e). Therefore, the theoretical development described in Sect. 6.3 for two-site square lattice can be also adopted here. In this sense, the NN-sites with non-null hopping are:  $\mathbf{d}_1 = (a, 0)$ ,  $\mathbf{d}_2 = (0, a)$  and  $\mathbf{d}_3 = (0, -a)$ . Thus, the transfer integral matrix elements are  $\mathcal{H}_{AA} = \epsilon_A$ ,  $\mathcal{H}_{BB} = \epsilon_B$  and

$$\begin{aligned}\mathcal{H}_{AB} &= \frac{1}{N} \left( Nt \sum_{n=1}^3 e^{i\mathbf{k} \cdot \mathbf{d}_n} \right) \\ &= t[e^{ik_x a} + 2 \cos(k_y a)] \\ &= \mathcal{H}_{BA}^*,\end{aligned}\quad (71)$$

and the overlap matrix elements are  $S_{AA} = 1$ ,  $S_{BB} = 1$  and

$$\begin{aligned}\mathcal{S}_{AB} &= \frac{1}{N} \left( Ns \sum_{n=1}^3 e^{i\mathbf{k} \cdot \mathbf{d}_n} \right) \\ &= s[e^{ik_x a} + 2 \cos(k_y a)] \\ &= \mathcal{S}_{BA}^*.\end{aligned}\quad (72)$$

Diagonalizing the secular Eq. (22) for the brick lattice by using Eqs. (71) and (72) and taking  $\epsilon_A = \epsilon_B = \epsilon_0$ , it results

$$E_{\pm}(\mathbf{k}) = \frac{\epsilon_0 \pm |\mathcal{H}_{AB}|}{1 \pm |\mathcal{S}_{AB}|}, \quad (73)$$

where

$$\begin{aligned}\frac{|\mathcal{H}_{AB}|}{t} &= \sqrt{3 + 2 \cos(2k_y a) + 4 \cos(k_y a) \cos(k_x a)} \\ &= \frac{|\mathcal{S}_{AB}|}{s}.\end{aligned}\quad (74)$$

Figures 4(c) and 5(b) present the energy spectrum of brick lattice along the high symmetry points of square lattice with two sites per unit cell (as in Fig. 4(b)), adding  $\mathbf{K}' = (0, 2\pi/3a)$ , i.e., it is shown along the  $\Gamma - \mathbf{M} - \mathbf{Y} - \mathbf{K}' - \Gamma$ -path and displayed along high symmetry points  $\Gamma = (0, 0)$ ,  $\mathbf{M} = (\pi/a, 0)$  and  $\mathbf{K} = (\pi/a, \pi/3a)$ , i.e., it is plotted along the  $\Gamma - \mathbf{M} - \mathbf{K} - \Gamma$ -path, which allows us to highlight the similarities with the two-site square lattice energy spectrum (Fig. 4(b)) and the graphene energy spectrum (Fig. 4(d)), respectively, as for instance, a non-dispersive behavior between  $\mathbf{M}$  and  $\mathbf{Y}$  points in a similar way to the square lattice case. Right panels in Fig. 4(c) show the contour plots of the conduction band for overlap parameter  $s = 0$  and  $s \neq 0$ . Dashed gray and black lines denote the first Brillouin zone and  $k$ -space direction adopted to the 2D plot in the left panel of 4(c), respectively. Comparing the energy levels and DOS of brick lattice (Fig. 4(c)) and graphene (Fig. 4(d)), it is clear to note the existence of the two Dirac cones within the first Brillouin zone, two peaks in DOS associated with the van Hove singularities, and a null DOS value at  $E = 0$ . The main difference is that the energy spectrum of brick lattice is strained in comparison with the graphene spectrum, such that the positions of the high symmetry points in  $k$ -space for brick lattice are not the same as the graphene ones, leading for instance a short distance between  $\mathbf{M} - \mathbf{K}$  points on brick lattice than in graphene, but in general the qualitative shape of both spectra is equivalent. Analyzing the role of the nonzero overlap parameter into the energy spectrum and DOS shown in Figs. 4(c) and 5(b), one can verify, similarly to the previous discussed lattice cases here, that  $s \neq 0$  leads to an electron–hole symmetry breaking and an unbalance between the amount of positive and negative energy states.

## 6.6 Brick Lattice in the Second Quantization

The second quantization Hamiltonian for the crystallographic structure of brick lattice can be read as

$$\hat{\mathcal{H}} = \sum_i \epsilon_A a_i^\dagger a_i + \sum_j \epsilon_B b_j^\dagger b_j + \sum_{i,j} t(a_i^\dagger b_j + b_j^\dagger a_i), \quad (75)$$

where  $\epsilon_{A(B)}$  and  $t$  are the on-site energy at  $A(B)$  sublattice and the NN hopping energy, respectively, as similarly defined in Eq. (55). To obtain the energy bands of this crystal structure, one can apply the discrete Fourier transforms (31)–(32) to write Eq. (75) in  $k$ -space, such as

$$\hat{\mathcal{H}} = \sum_{\mathbf{k}} [\epsilon_0 (a_{\mathbf{k}}^\dagger a_{\mathbf{k}} + b_{\mathbf{k}}^\dagger b_{\mathbf{k}}) + t (a_{\mathbf{k}}^\dagger f(\mathbf{k}) b_{\mathbf{k}} + b_{\mathbf{k}}^\dagger f(\mathbf{k})^* a_{\mathbf{k}})], \quad (76)$$

where we assumed  $\epsilon_A = \epsilon_B = \epsilon_0$ .  $f(\mathbf{k})$  is the geometric structure factor given by

$$f(\mathbf{k}) = [e^{ik_x a} + 2 \cos(k_y a)]. \quad (77)$$

Thus, Eq. (76) can be rewritten as

$$\hat{\mathcal{H}} = \sum_{\mathbf{k}} \langle \Psi_{\mathbf{k}} | \mathcal{H} | \Psi_{\mathbf{k}} \rangle, \quad (78)$$

and the energy bands are obtained by diagonalizing  $\mathcal{H}$  in Eq. (78), resulting in the following expression:

$$E_{\pm}(\mathbf{k}) = \epsilon_0 \pm t \sqrt{3 + 2 \cos(2k_y a) + 4 \cos(k_y a) \cos(k_x a)}, \quad (79)$$

with the energy spectrum being depicted in Figs. 4(c) and 5(b).

## 6.7 Graphene in the First Quantization

After discussed in Sect. 6.5 the brick lattice, a topological equivalent lattice to graphene, let us now calculate the energy bands of the honeycomb lattice structure describing a monolayer graphite, i.e., a 2D crystal named graphene, by means of the first and second quantization formalism. The honeycomb structure of graphene is not a Bravais lattice. However, it can be described as two interpenetrating triangular Bravais sublattices, namely  $A$  and  $B$  sublattices, as shown in Fig. 1(e), i.e., it has two sites ( $A$  and  $B$ ) per unit cell. Each carbon atom of sublattice  $A$  ( $B$ ) has three NN carbon atoms of sublattice  $B$  ( $A$ ). The NNN sites of a carbon atom of a given sublattice, in turn, are six carbon atoms of the same sublattice. The hopping parameter between NN sites is approximately an order of magnitude greater than that between NNN sites [32]. In that sense, we can safely neglect the interactions beyond NNN sites. The primitive vectors of graphene real lattice are  $\mathbf{a}_1 = (3a/2, \sqrt{3}a/2)$  and  $\mathbf{a}_2 = (3a/2, -\sqrt{3}a/2)$ , so that the primitive vectors of the reciprocal lattice, shown in Fig. 2(e), are  $\mathbf{b}_1 = [2\pi/(3a), 2\pi\sqrt{3}/(3a)]$  and  $\mathbf{b}_2 = [2\pi/(3a), -2\pi\sqrt{3}/(3a)]$ . The first Brillouin zone [highlighted by the yellow region in Fig. 2(e)] is a hexagon limited by  $\mathbf{K}_1 = [2\pi/(3a), 2\pi/(3\sqrt{3}a)]$ ,  $\mathbf{K}_2 = [2\pi/(3a), -2\pi/(3\sqrt{3}a)]$ ,  $\mathbf{K}_3 = [0, -4\pi/(3\sqrt{3}a)]$ ,  $\mathbf{K}_4 = [-2\pi/(3a), -2\pi/(3\sqrt{3}a)]$ ,  $\mathbf{K}_5 = [-2\pi/(3a), 2\pi/(3\sqrt{3}a)]$  and  $\mathbf{K}_6 = [0, 4\pi/(3\sqrt{3}a)]$ . Of these six points, only two are not equivalent and are called

Dirac points. Thus, the Bloch function consisting of  $A$  and  $B$  sites is written as

$$\Phi_j(\mathbf{r}, \mathbf{k}) = \frac{1}{\sqrt{N}} \sum_{\mathbf{R}_{\alpha}} e^{i\mathbf{k}\cdot\mathbf{R}_{\alpha}} \varphi_j(\mathbf{r} - \mathbf{R}_{\alpha}), \quad \alpha = (A, B). \quad (80)$$

The transfer integral and overlap matrices are given by

$$\mathcal{H} = \begin{pmatrix} \mathcal{H}_{AA} & \mathcal{H}_{AB} \\ \mathcal{H}_{BA} & \mathcal{H}_{BB} \end{pmatrix} \quad \text{and} \quad S = \begin{pmatrix} \mathcal{S}_{AA} & \mathcal{S}_{AB} \\ \mathcal{S}_{BA} & \mathcal{S}_{BB} \end{pmatrix}, \quad (81)$$

with the  $\mathcal{H}$  elements being  $\mathcal{H}_{AA} = \epsilon_A$ ,  $\mathcal{H}_{BB} = \epsilon_B$  and

$$\begin{aligned} \mathcal{H}_{AB} &= \frac{1}{N} \left( Nt \sum_{n=1}^3 e^{i\mathbf{k}\cdot\mathbf{d}_n} \right) \\ &= t \left[ e^{ik_x a} + 2e^{-ik_x a/2} \cos(k_y a \sqrt{3}/2) \right] \\ &= \mathcal{H}_{BA}^*, \end{aligned} \quad (82)$$

with NN sites localized by the vectors  $\mathbf{d}_1 = (a, 0)$ ,  $\mathbf{d}_2 = (-a/2, a\sqrt{3}/2)$  and  $\mathbf{d}_3 = (-a/2, -a\sqrt{3}/2)$ . Likewise, the overlap matrix elements are  $\mathcal{S}_{AA} = 1$ ,  $\mathcal{S}_{BB} = 1$  and

$$\begin{aligned} \mathcal{S}_{AB} &= \frac{1}{N} \left( Ns \sum_{n=1}^3 e^{i\mathbf{k}\cdot\mathbf{d}_n} \right) \\ &= s \left[ e^{ik_x a} + 2e^{-ik_x a/2} \cos(k_y a \sqrt{3}/2) \right] \\ &= \mathcal{S}_{BA}^*. \end{aligned} \quad (83)$$

Since  $A$  and  $B$  sites are identical carbon atoms,  $\epsilon_A = \epsilon_B = \epsilon_0$ , and the secular Eq. (22) for graphene can be written as

$$\det \begin{bmatrix} \epsilon_0 - E_{\pm}(\mathbf{k}) & \mathcal{H}_{AB} - E_{\pm}(\mathbf{k})\mathcal{S}_{AB} \\ \mathcal{H}_{AB}^* - E_{\pm}(\mathbf{k})\mathcal{S}_{AB}^* & \epsilon_0 - E_{\pm}(\mathbf{k}) \end{bmatrix} = 0, \quad (84)$$

resulting in the following dispersion relation:

$$E_{\pm}(\mathbf{k}) = \frac{\epsilon_0 \pm |\mathcal{H}_{AB}|}{1 \pm |\mathcal{S}_{AB}|}, \quad (85)$$

where

$$\begin{aligned} &\sqrt{3 + 2 \cos(\sqrt{3}k_y a) + 4 \cos\left(\frac{\sqrt{3}k_y a}{2}\right) \cos\left(\frac{3k_x a}{2}\right)} \\ &= \frac{|\mathcal{H}_{AB}|}{t} = \frac{|\mathcal{S}_{AB}|}{s}, \end{aligned} \quad (86)$$

where  $E_{-}(\mathbf{k})$  and  $E_{+}(\mathbf{k})$  refer to the valence and conduction bands of graphene, respectively. By comparing Eqs. (70)–(71) with Eqs. (85)–(86), one realizes the strong similarity between the obtained dispersion relations for brick lattice and graphene, respectively, such that these lattices can be mapped one in the other by the following  $k$ -space transformation:  $(k_x^b, k_y^b) \rightarrow (3k_x^g/2, \sqrt{3}k_y^g/2)$ , with the superscripts  $g$

and  $b$  referring to brick and graphene lattices. Consequently, the position of the high symmetry points in the reciprocal space is changed by a factor of  $\sqrt{3}/2$  and  $3/2$  along the  $x$  and  $y$  directions, respectively, with respect to the graphene case, as discussed in Sect. 6.5, and the energy spectrum of the brick lattice looks anisotropic, whereas the graphene bands are isotropic (see contour plots shown in Fig. 4(c) and (d)). The graphene energy spectrum is shown in Fig. 4(d) along the  $\Gamma - \mathbf{M} - \mathbf{K} - \Gamma$ -path, as illustrated by the dashed black line in the inset of the contour plot on the right panel of Fig. 4(d). Note that there are six points where conduction and valence bands touch (see red spots in the contour plot); of these six points, only two are non-equivalent, which are called as Dirac points ( $\mathbf{K}$  and  $\mathbf{K}'$ ). This gapless band structure feature of graphene leads to its characterization as a semimetal. Low-energy charge carriers in graphene behave like massless Dirac fermions near the Fermi level [33], where the energy–wavevector dispersion relationship is linear, i.e.,  $E(k) \propto k$ . That is demonstrated by expanding the TB Hamiltonian around the Dirac points [32], obtaining a continuum Hamiltonian within the long-wavelength approximation. As before, the nonzero overlap parameter causes electron–hole symmetry breaking on energy spectrum and an energy unbalance in the DOS with respect to zero energy.

## 6.8 Graphene in the Second Quantization

The procedure below is very similar to the one described in Sect. 6.6 for brick lattice, due to the topological equivalence between the graphene and brick lattices. The Hamiltonian of graphene in the second quantization is the same as Eq. (75), such as

$$\hat{\mathcal{H}} = \sum_i \epsilon_A a_i^\dagger a_i + \sum_j \epsilon_B b_j^\dagger b_j + \sum_{ij} t(a_i^\dagger b_j + b_j^\dagger a_i), \quad (87)$$

where  $\epsilon_A$ ,  $\epsilon_B$  and  $t$  have the same definitions as Eq. (55), referring to the on-site energies in the sublattices  $A$  and  $B$ , and the NN hopping energy between  $A - B$  sublattices, respectively. To obtain the energy bands of graphene, we can apply the discrete Fourier transforms (31)–(32) to rewrite  $\hat{\mathcal{H}}$  of Eq. (90) as

$$\hat{\mathcal{H}} = \sum_{\mathbf{k}} [a_{\mathbf{k}}^\dagger \epsilon_0 a_{\mathbf{k}} + b_{\mathbf{k}}^\dagger \epsilon_0 b_{\mathbf{k}} + a_{\mathbf{k}}^\dagger t f(\mathbf{k}) b_{\mathbf{k}} + b_{\mathbf{k}}^\dagger t f(\mathbf{k})^* a_{\mathbf{k}}], \quad (88)$$

where it was taken  $\epsilon_A = \epsilon_B = \epsilon_0$ . The geometric structure factor  $f(\mathbf{k}) = \sum_{n=1}^3 e^{i\mathbf{k}\cdot\mathbf{d}_n}$  can be explicitly written as

$$f(\mathbf{k}) = [e^{ik_x a} + 2e^{-ik_x a/2} \cos(k_y a \sqrt{3}/2)]. \quad (89)$$

In matrix format, Eq. (88) reads as

$$\begin{aligned} \hat{\mathcal{H}} &= \sum_{\mathbf{k}} [a_{\mathbf{k}}^\dagger \ b_{\mathbf{k}}^\dagger] \begin{bmatrix} \epsilon_0 & t f(\mathbf{k}) \\ t f(\mathbf{k})^* & \epsilon_0 \end{bmatrix} \begin{bmatrix} a_{\mathbf{k}} \\ b_{\mathbf{k}} \end{bmatrix} \\ &= \sum_{\mathbf{k}} \langle \Psi_{\mathbf{k}} | \mathcal{H} | \Psi_{\mathbf{k}} \rangle. \end{aligned} \quad (90)$$

Note that the wave function  $|\Psi\rangle = [\Psi_A, \Psi_B]^T$  is a two-component pseudospinor, i.e., a  $1 \times 2$  column matrix, where  $\Psi_{A(B)}$  are the envelop functions associated with the electron probabilities in  $A(B)$  sublattices. Diagonalizing  $\mathcal{H}$  in Eq. (90), one obtains the graphene dispersion relation

$$E_{\pm}(\mathbf{k}) \epsilon_0 \pm t \sqrt{3 + 2 \cos(\sqrt{3}k_y a) + 4 \cos\left(\frac{\sqrt{3}k_y a}{2}\right)\left(\frac{3k_x a}{2}\right)}. \quad (91)$$

depicted in Fig. 4(d) and discussed in Sect. 6.7.

## 6.9 $\tau_3$ -lattice in the First Quantization

Starting from the honeycomb lattice with two sites ( $A$  and  $B$ ) per unit cell, the  $\tau_3$ -lattice or Dice lattice [34] is obtained by connecting additional ( $C$ ) sites at the center of each hexagon to the  $B$  sites (see Fig. 1(g)). The  $\tau_3$ -lattice is thus a triangular Bravais lattice with three sites per unit cell, i.e., it can be described as three interpenetrating triangular Bravais sublattices, namely  $A$ ,  $B$  and  $C$  sublattices. Each site of  $A$  ( $B$ ) sublattice has three NN sites of  $B$  ( $A$ ) sublattice, and each site of  $B$  ( $C$ ) sublattice has three NN sites of  $C$  ( $B$ ) sublattice. The hopping between  $A$  and  $C$  sites is disregarded because they are not connected. The primitive vectors of the real lattice are the same as the ones for graphene:  $\mathbf{a}_1 = (3a/2, \sqrt{3}a/2)$  and  $\mathbf{a}_2 = (3a/2, -\sqrt{3}a/2)$ , so that the primitive vectors of the reciprocal lattice, shown in Fig. 2(e), are  $\mathbf{b}_1 = [2\pi/(3a), 2\pi\sqrt{3}/(3a)]$  and  $\mathbf{b}_2 = [2\pi/(3a), -2\pi\sqrt{3}/(3a)]$ . The first Brillouin zone is equal to that of graphene discussed in Sect. 6.7 (see Fig. 2(e)). Thus, the Bloch function consisting of  $A$ ,  $B$  and  $C$  sites is written as

$$\Phi_j(\mathbf{r}, \mathbf{k}) = \frac{1}{\sqrt{N}} \sum_{\mathbf{R}_{\alpha}} e^{i\mathbf{k}\cdot\mathbf{R}_{\alpha}} \varphi_j(\mathbf{r} - \mathbf{R}_{\alpha}), \quad \alpha = (A, B, C). \quad (92)$$

So that the transfer integral and overlap matrices are given by

$$\mathcal{H} = \begin{pmatrix} \mathcal{H}_{AA} & \mathcal{H}_{AB} & \mathcal{H}_{AC} \\ \mathcal{H}_{BA} & \mathcal{H}_{BB} & \mathcal{H}_{BC} \\ \mathcal{H}_{CA} & \mathcal{H}_{CB} & \mathcal{H}_{CC} \end{pmatrix}, \quad S = \begin{pmatrix} S_{AA} & S_{AB} & S_{AC} \\ S_{BA} & S_{BB} & S_{BC} \\ S_{CA} & S_{CB} & S_{CC} \end{pmatrix}, \quad (93)$$

where the transfer integral matrix elements are  $\mathcal{H}_{AA} = \epsilon_A$ ,  $\mathcal{H}_{BB} = \epsilon_B$ ,  $\mathcal{H}_{CC} = \epsilon_C$ ,  $\mathcal{H}_{BC} = \mathcal{H}_{AB}$ ,  $\mathcal{H}_{CB} = \mathcal{H}_{AB}^*$  and

$$\begin{aligned}\mathcal{H}_{AB} &= \frac{1}{N} \left( Nt \sum_{n=1}^3 e^{i\mathbf{k} \cdot \mathbf{d}_n} \right) \\ &= t \left[ e^{ik_x a} + 2e^{-ik_x a/2} \cos(k_y a \sqrt{3}/2) \right] \\ &= \mathcal{H}_{BA}^*,\end{aligned}\quad (94)$$

with NN sites being localized by the vectors  $\mathbf{d}_1 = (a, 0)$ ,  $\mathbf{d}_2 = (-a/2, a\sqrt{3}/2)$  and  $\mathbf{d}_3 = (-a/2, -a\sqrt{3}/2)$ . Likewise, the overlap matrix elements are  $S_{AA} = 1$ ,  $S_{BB} = 1$ ,  $S_{CC} = 1$ ,  $S_{BC} = S_{AB}$ ,  $S_{CB} = S_{AB}^*$  and

$$\begin{aligned}\mathcal{S}_{AB} &= \frac{1}{N} \left( Ns \sum_{n=1}^3 e^{i\mathbf{k} \cdot \mathbf{d}_n} \right) \\ &= s \left[ e^{ik_x a} + 2e^{-ik_x a/2} \cos(k_y a \sqrt{3}/2) \right] \\ &= \mathcal{S}_{BA}^*.\end{aligned}\quad (95)$$

For simplicity, let us admit that  $\epsilon_A = \epsilon_B = \epsilon_C = \epsilon_0$ . Therefore, the secular Eq. (22) with the use of the transfer integral and overlap matrices given by Eqs. (94) and (95) results in

$$\det \begin{bmatrix} \epsilon_0 - E_i(\mathbf{k}) & \mathcal{H}_{AB} - E_i(\mathbf{k})\mathcal{S}_{AB} & 0 \\ \mathcal{H}_{AB}^* - E_i(\mathbf{k})\mathcal{S}_{AB}^* & \epsilon_0 - E_i(\mathbf{k}) & \mathcal{H}_{AB} - E_i(\mathbf{k})\mathcal{S}_{AB} \\ 0 & \mathcal{H}_{AB}^* - E_i(\mathbf{k})\mathcal{S}_{AB}^* & \epsilon_0 - E_i(\mathbf{k}) \end{bmatrix} = 0,\quad (96)$$

whose solution is given by

$$E_0 = 0,\quad (97)$$

$$E_{\pm}(\mathbf{k}) = \frac{\epsilon_0 \pm \sqrt{2}|\mathcal{H}_{AB}|}{1 \pm \sqrt{2}|\mathcal{S}_{AB}|},\quad (98)$$

where

$$\begin{aligned}&\sqrt{3 + 2 \cos(\sqrt{3}k_y a) + 4 \cos\left(\frac{\sqrt{3}k_y a}{2}\right)} \cos\left(\frac{3k_x a}{2}\right) \\ &= \frac{|\mathcal{H}_{AB}|}{t} = \frac{|\mathcal{S}_{AB}|}{s}.\end{aligned}\quad (99)$$

Since  $\tau_3$ -lattice consists of a crystallographic structure with three sites per unit cell, its energy spectrum is composed by three energy bands:  $E_+(\mathbf{k})$ ,  $E_0$  and  $E_-(\mathbf{k})$ , referring to the bottom, middle and top bands, respectively. Note that the terms  $|\mathcal{H}_{AB}|/t$  and  $|\mathcal{S}_{AB}|/s$  in Eq. (86) for graphene and in Eq. (99) for  $\tau_3$ -lattice are exactly the same, whereas the  $E_{\pm}(\mathbf{k})$  bands for graphene in Eq. (85) and for  $\tau_3$ -lattice in Eq. (98) differ by the presence of a  $\sqrt{2}$  term multiplying  $|\mathcal{H}_{AB}|$  in the numerator and multiplying  $|\mathcal{S}_{AB}|$  in the denominator. In addition to the two bands ( $E_{\pm}(\mathbf{k})$ ) similar to the graphene ones, the particularity of the  $\tau_3$ -lattice energy spectrum is the

flat band  $E_0 = 0$ . Figure 4(e) shows the energy spectrum and DOS of  $\tau_3$ -lattice along the same  $k$ -space direction as in the graphene case to a better comparison between them, and as also illustrated by the dashed black line in the inset of the contour plot in the right panel of Fig. 4(e). As in graphene, there are six points where the valence and conduction bands touch, which are triply degenerate due to the presence of the flat band. Owing to this non-dispersive band, the DOS for  $\tau_3$ -lattice exhibits an extra peak at  $E = 0$  in comparison with graphene that has two peaks associated with the van Hove singularities. Furthermore, again one can realize that the nonzero overlap parameter causes electron–hole symmetry breaking and the energy spectrum seems to be shifted up.

## 6.10 $\tau_3$ -lattice in the Second Quantization

The Hamiltonian of  $\tau_3$ -lattice in the second quantization can be written as

$$\begin{aligned}\hat{\mathcal{H}} = & \sum_i \epsilon_A a_i^\dagger a_i + \sum_j \epsilon_B b_j^\dagger b_j + \sum_k \epsilon_C c_k^\dagger c_k \\ & + \sum_{i,j} t(b_j^\dagger a_i + a_i^\dagger b_j) + \sum_{j,k} t(b_j^\dagger c_k + c_k^\dagger b_j),\end{aligned}\quad (100)$$

where  $\epsilon_A$ ,  $\epsilon_B$  and  $\epsilon_C$  represent the on-site energies on sites of type A, B and C, respectively.  $t$  is defined as the hopping parameter between NN sites  $A - B$  and  $B - C$ . To obtain the energy bands of  $\tau_3$ -lattice, we repeat the same procedure done for the previous investigated lattices, applying the discrete Fourier transforms (31)–(32) and taking  $\epsilon_A = \epsilon_B = \epsilon_C = \epsilon_0$  to rewrite Eq. (100) as

$$\begin{aligned}\hat{\mathcal{H}} = & \sum_{\mathbf{k}} [a_{\mathbf{k}}^\dagger \epsilon_0 a_{\mathbf{k}} + b_{\mathbf{k}}^\dagger \epsilon_0 b_{\mathbf{k}} + c_{\mathbf{k}}^\dagger \epsilon_0 c_{\mathbf{k}} + a_{\mathbf{k}}^\dagger t f(\mathbf{k}) b_{\mathbf{k}} \\ & + b_{\mathbf{k}}^\dagger t f(\mathbf{k})^* a_{\mathbf{k}} + b_{\mathbf{k}}^\dagger t f(\mathbf{k}) c_{\mathbf{k}} + c_{\mathbf{k}}^\dagger t f(\mathbf{k})^* b_{\mathbf{k}}],\end{aligned}\quad (101)$$

with the geometric structure factor being  $f(\mathbf{k}) = \sum_{n=1}^3 e^{i\mathbf{k} \cdot \mathbf{d}_n}$  or, explicitly

$$f(\mathbf{k}) = \left[ e^{ik_x a} + 2e^{-ik_x a/2} \cos(k_y a \sqrt{3}/2) \right].\quad (102)$$

Rewriting Eq. (101) in a matrix form, one gets

$$\begin{aligned}\hat{\mathcal{H}} = & \sum_{\mathbf{k}} [a_{\mathbf{k}}^\dagger \ b_{\mathbf{k}}^\dagger \ c_{\mathbf{k}}^\dagger] \begin{bmatrix} \epsilon_0 & t f(\mathbf{k}) & 0 \\ t f(\mathbf{k})^* & \epsilon_0 & t f(\mathbf{k}) \\ 0 & t f(\mathbf{k})^* & \epsilon_0 \end{bmatrix} \begin{bmatrix} a_{\mathbf{k}} \\ b_{\mathbf{k}} \\ c_{\mathbf{k}} \end{bmatrix} \\ & = \sum_{\mathbf{k}} \langle \Psi_{\mathbf{k}} | \mathcal{H} | \Psi_{\mathbf{k}} \rangle.\end{aligned}\quad (103)$$

The corresponding energy bands of  $\tau_3$ -lattice are calculated by diagonalizing  $\mathcal{H}$  in Eq. (103) (see Fig. 4(e)), resulting in  $E_0 = 0$ ,  $E_{\pm}(\mathbf{k})$  and  $E_{\pm}(\mathbf{k})$  for the bottom, middle and top bands, respectively. The energy bands of  $\tau_3$ -lattice are shown in Fig. 4(e) for comparison with the corresponding bands of graphene.

$$E_{\pm}(\mathbf{k}) = \epsilon_0 \pm t \sqrt{3 + 2 \cos(\sqrt{3}k_y a) + 4 \cos\left(\frac{\sqrt{3}k_y a}{2}\right) \cos\left(\frac{3k_x a}{2}\right)}. \quad (105)$$

## 7 Conclusion

We have shown how the TB model can be applied to the study of the electronic band structure of several periodic structures. The model can be applied to a wide range of systems, such as molecules, polymers, nanotubes and 2D and 3D crystals, and we presented calculations for the energy spectrum for 2D systems with one, two and three bands of energy. A nonzero overlap parameter showed to cause electron–hole symmetry breaking of the energy spectrum and an energetic unbalance in the DOS with respect to zero energy.

Furthermore, the results highlighted the fact that many of the distinct properties of these systems, such as the linear dispersion of electrons close to the Fermi level in graphene and the flat band of  $\tau_3$ -lattice, are mainly a consequence of the geometry of the lattice and the number of non-equivalent sublattices. However, these spectra can be significantly modified by the inclusion of additional effects such as electron–electron interaction, which can be introduced in a first approximation by the addition of a mean-field Hubbard term in the Hamiltonian. Another possible addition to the model is the inclusion of the spin-orbit coupling, which can lead to the formation of a gap in the spectrum. Moreover, the model can be easily modified to deal with the presence of surfaces and edges. In that case, as the system loses translation symmetry along one direction, and also due to possible on-site energies or hopping modifications due to the absence of bonds, the model may give rise to surface- or edge-localized states. These states have been intensively investigated in connection with topological effects in materials. A further modification is the addition of lattice defects or impurities, which cause the formation of non-propagating localized states. Each addition to the model increases the complexity of the calculations necessary for obtaining the spectra, which can then be tackled by numerical approaches.

**Acknowledgements** Discussions with André J. Chaves are gratefully acknowledged. The authors are grateful to Conselho Nacional de Desenvolvimento Científico e Tecnológico (CNPq), to Coordenação de Aperfeiçoamento de Pessoal de Nível Superior (CAPES) of Brazil for financial support, and to Fundação Cearense de Apoio ao Desenvolvimento Científico e Tecnológico (FUNCAP). D.R.C is supported by CNPq grant numbers 310019/2018-4 and 437067/2018-1. J.M.P.Jr. and D.R.C are supported by bilateral ITA-UFC CNPq project number 400879/2019-0.

## References

- P. Hohenberg, W. Kohn, Phys. Rev. **136**, B864 (1964)
- F. Bloch, Zeitschrift für physik **52**(7), 555 (1929)
- J.C. Slater, G.F. Koster, Phys. Rev. **94**(6), 1498 (1954)
- K.S. Novoselov, A.K. Geim, S.V. Morozov, D. Jiang, Y. Zhang, S.V. Dubonos, I.V. Grigorieva, A.A. Firsov, Science **306**, 666 (2004)
- A. Rudenko, S. Yuan, M. Katsnelson, Phys. Rev. B **92**(8), 085419 (2015)
- S. Reich, J. Maultzsch, C. Thomsen, P. Ordejon, Phys. Rev. B **66**(3), 035412 (2002)
- A.V. Gert, M.O. Nestoklon, I.N. Yassievich, J. Exp. Theor. Phys. **121**(1), 115 (2015)
- R.M. Ribeiro, N.M.R. Peres, Phys. Rev. B **83**(23), 235312 (2011)
- K. Tagami, M. Tsukada, T. Matsumoto, T. Kawai, Phys. Rev. B **67**(24), 245324 (2003)
- Y. Liu, P. Hui, Phys. Rev. B **57**(20), 12994 (1998)
- J.A. Fürst, J. Hashemi, T. Markussen, M. Brandbyge, A.-P. Jauho, R.M. Nieminen, Phys. Rev. B **80**(3), 035427 (2009)
- F.R.V. Araújo, D.R. da Costa, A.C.S. Nascimento, J.M. Pereira Jr., J. Phys. Condens. Matter **32**(42), 425501 (2020)
- F.R.V. Araújo, D.R. da Costa, F.N. Lima, A.C.S. Nascimento, J.M. Pereira Jr., J. Phys. Condens. Matter **33**(37), 375501 (2021)
- K.H. Ding, L.K. Lim, G. Su, Z.Y. Weng, Phys. Rev. B **97**(3), 035123 (2018)
- N.W. Ashcroft, N.D. Mermin, *Solid State Physics* (Saunders College, Philadelphia, 1976)
- G. Dresselhaus, M.S. Dresselhaus, R. Saito, *Physical properties of carbon nanotubes* (World scientific, Singapore, 1998)
- Note that the method's name referred here as transfer matrix is also given to another method associated with scattering problems in quantum mechanics and electromagnetism (see Ref. [18])
- P. Markos, C.M. Soukoulis, *Wave Propagation: From Electrons to Photonic Crystals and Left-Handed Materials* (Princeton University Press, Princeton, 2008)
- M.P. Marder, *Condensed Matter Physics* (John Wiley & Sons, New York, 2010)
- K.F. Garrity, K. Choudhary, Sci. Data **8**, 1 (2021)
- A.L. Fetter, J.D. Walecka, *Quantum theory of many-particle systems* (Courier Corporation, New York, 2012)
- I.S. Oliveira, V.L.B. De Jesus, *Introdução à física do estado sólido* (Editora Livraria da Física, São Paulo, 2005)
- C. Kittel, P. McEuen, P. McEuen, *Introduction to solid state physics*, vol. 8 (Wiley, New York, 1996)
- D.R. da Costa, M. Zarenia, A. Chaves, G.A. Farias, F.M. Peeters, Phys. Rev. B **92**(11), 115437 (2015)
- R. Kundu, Mod. Phys. Lett. B **25**(03), 163 (2011)
- B.A. McKinnon, T.C. Choy, Phys. Rev. B **52**(20), 14531 (1995)
- K. Wakabayashi, M. Fujita, H. Ajiki, M. Sigrist, Phys. Rev. B **59**(12), 8271 (1999)
- G. Montambaux, C. R. Phys. **19**(5), 285 (2018)
- J.M. Hou, W. Chen, Sci. Rep. **5**(1), 1 (2015)
- D.A. Abanin, T. Kitagawa, I. Bloch, E. Demler, Phys. Rev. Lett. **110**(16), 165304 (2013)
- E.T. Sisakht, M.H. Zare, F. Fazileh, Phys. Rev. B **91**(8), 085409 (2015)
- A.H.C. Neto, F. Guinea, N.M.R. Peres, K.S. Novoselov, A.K. Geim, Rev. Mod. Phys. **81**, 109 (2009)
- K.S. Novoselov, A.K. Geim, S.V. Morozov, D. Jiang, M.I. Katsnelson, I. Grigorieva, S.V.B. Dubonos, A.A. Firsov, Nature **438**, 197 (2005)
- F. Piéchon, J.N. Fuchs, A. Raoux, G. Montambaux, J. Phys. Conf. Ser. **603**, 012001 (2015)
- A. Beggi, I. Siloi, C. Benedetti, E. Piccinini, L. Razzoli, P. Bordone, M.G. Paris, Eur. J. Phys. **39**(6), 065401 (2018)

**Publisher's Note** Springer Nature remains neutral with regard to jurisdictional claims in published maps and institutional affiliations.